



# Laser ignition chemical synthesis of bulk $\text{Al}_2\text{O}_3$ - $\text{TiB}_2$ composites for impact resistance application

Evangelos Daskalakis<sup>a,\*</sup>, Andrew Scott<sup>a</sup>, Rebecca Mangham<sup>b</sup>, Neil Middleton<sup>b</sup>, Animesh Jha<sup>a</sup>

<sup>a</sup> School of Chemical and Process Engineering, University of Leeds, Leeds, LS2 9JT, UK

<sup>b</sup> Physical Sciences Group, Defence Science and Technology Laboratory, SP4 0JQ, UK

## ARTICLE INFO

Handling editor: L Murr

### Keywords:

Laser ignition chemical synthesis  
Energy efficiency  
Ceramic composites  
Self-sustaining reaction  
Keyhole  
Marangoni convection

## ABSTRACT

The increasing demand for advanced materials has prompted the exploration of energy-efficient processes for near-net shape manufacturing. Laser ignition chemical synthesis (LiChemS) is a novel technology for rapid and cost-effective synthesis of refractory materials. Using a 976 nm quasi-CW diode laser, we manufactured  $\text{Al}_2\text{O}_3$ - $\text{TiB}_2$  composites in situ from aluminum,  $\text{TiO}_2$ , and  $\text{B}_2\text{O}_3$ . Leveraging low-power laser processing and an exotherm-driven mechanism, which involves keyhole formation, metal vapour ionisation, and Marangoni convection, LiChemS generated plasma for propagating the reaction across the bulk, for laser intensity of 1.13 W/ $\text{mm}^2$ . The adiabatic temperature and activation energy of LiChemS were calculated as 2643 K and 11.6 kJ/mol respectively. A Newtonian cooling model predicted crack generation within the composites for a differential temperature of 349 K between the centre and edges. We propose a new reaction mechanism yielding high-purity composites, displaying only traces of  $\text{Ti}_2\text{O}_3$ . The composites exhibited skeletal and bulk densities of 4010  $\text{kg}/\text{m}^3$  (96 %) and 3830  $\text{kg}/\text{m}^3$  (92 %) respectively, fracture toughness of 5.8  $\text{MPa m}^{1/2}$ , and Vickers microhardness of  $18.14 \pm 0.49$  GPa. The optimum  $\text{Al}_2\text{O}_3$ - $\text{TiB}_2$  composite demonstrated 15 % greater compressive strength than monolithic alumina and withstood 174 N before fracturing. An analytical model combining Hertzian contact mechanics with impact mechanics correlated the ball-drop heights during impact testing to the defect sizes within the composites. The composites presented a surface roughness of 14.9  $\mu\text{m}$  and fine dispersion of  $\text{TiB}_2$  and  $\text{Ti}_2\text{O}_3$  nanoparticles within the alumina matrix. The results herein suggest great scalability opportunities for LiChemS in manufacturing customised, high purity, energy demanding materials.

## Nomenclature

| Section 2.1      |                                                  | Section 3.4                |                                |
|------------------|--------------------------------------------------|----------------------------|--------------------------------|
| $C_{\text{air}}$ | Concentration of air remaining                   | ( $\mu$ )                  | linear attenuation coefficient |
| Co               | Starting concentration of Air                    | (x)                        | thickness of the material      |
| $n_{\text{air}}$ | Number of volume exchanges                       | Section 3.7                |                                |
| Section 2.2      |                                                  | HV                         | Vickers Hardness               |
| I                | laser intensity ( $\text{W}/\text{m}^2$ )        | c                          | Crack Length                   |
| P                | laser power (W)                                  | Discussion Section 4.5     |                                |
| $w_f$            | beam radius at the focal point (m)               | (Gc)                       | Critical energy release rate   |
| Section 2.3      |                                                  | (continued on next column) |                                |
| $t_{\text{dry}}$ | Time required for evaporating the absorbed water |                            |                                |

## (continued)

|                          |                                                   |
|--------------------------|---------------------------------------------------|
| $m_w$                    | mass of water                                     |
| $\lambda_w$              | latent heat of vaporization of water (2260 kJ/kg) |
| Section 2.6              |                                                   |
| $R_{\text{ssb}}$         | Radius of the stainless steel ball (m)            |
| F                        | Force (N)                                         |
| $E^*$                    | Effective elastic modulus                         |
| $\nu_{\text{ball}}$      | Poisson Ratio of stainless steel ball             |
| $\nu_{\text{composite}}$ | Poisson Ratio of composite                        |
| $\sigma_{\text{maxPO}}$  | Contact stress generated at impact                |
| ( $\sigma_C$ )           | Critical Stress                                   |
| $K_{\text{IC}}$          | Fracture toughness                                |

(continued on next page)

\* Corresponding author.

E-mail address: [e.daskalakis@leeds.ac.uk](mailto:e.daskalakis@leeds.ac.uk) (E. Daskalakis).

(continued)

|                   |                                                                      |
|-------------------|----------------------------------------------------------------------|
| $a_d$             | Defect size                                                          |
| U                 | Energy at impact                                                     |
| Vc                | Volume of composite                                                  |
| E                 | Young's Modulus                                                      |
| $h_{sf}$          | Height for surface fracture                                          |
| $h_{bf}$          | Height for bulk fracture                                             |
| Section 3.1       |                                                                      |
| A                 | Absorbance                                                           |
| R                 | Reflectance                                                          |
| T                 | Transmittance                                                        |
| a                 | Absorption coefficient                                               |
| d                 | Thickness of the pellet (3 mm)                                       |
| Section 3.2       |                                                                      |
| Q                 | Adiabatic Heat                                                       |
| $-\Delta H_{298}$ | Enthalpy of Reaction                                                 |
| $T_{ad}$          | Adiabatic Temperature (K)                                            |
| $T_{amb}$         | Room temperature (K)                                                 |
| h                 | convective heat transfer coefficient                                 |
| As                | Surface area ( $m^2$ )                                               |
| $\rho$            | Density ( $kg/m^3$ )                                                 |
| Cp                | specific heat capacity (J/gK)                                        |
| kf                | Thermal conductivity of argon gas W/(m·K)                            |
| g                 | Acceleration due to gravity ( $m/s^2$ )                              |
| $\beta$           | Coefficient of thermal expansion of argon ( $2 \times 10^{-3} 1/K$ ) |
| Lc                | Length of the composite (m)                                          |
| vk                | Kinematic viscosity of argon ( $m^2/s$ )                             |
| pf                | Density of argon ( $kg/m^3$ )                                        |
| $\mu$             | Dynamic viscosity of argon                                           |
| $a_{th}$          | Thermal expansion coefficient                                        |
| $\beta$           | Heating rate of the material (K/s)                                   |
| Tp                | Ignition temperature (K)                                             |
| R                 | Gas constant ( $J \cdot K^{-1} \cdot mol^{-1}$ )                     |
| Cp                | Specific Heat Capacity (J/kg·C)                                      |

## 1. Introduction

Ceramic matrix composites exhibit superior mechanical, thermal, and electrical properties compared to their base monolithic matrices. From the ceramic matrix composites, Alumina-TiB<sub>2</sub> stands out due to its superior hardness, thermal stability, toughness, and oxidation resistance which makes it suitable for aviation, aerospace, wear-resistant and impact resistance related applications [1]. Alumina is an insulator with a low thermal expansion coefficient, high thermal stability, and oxidation resistance, though it exhibits poor shock resistance [2], while TiB<sub>2</sub> demonstrates notable heat and electrical conductivity [3] and high fracture toughness. The hexagonal structure of TiB<sub>2</sub> features alternating metalically bonded Ti layers and covalently bonded boron layers, forming an ABAB stacking parallel to the basal plane [4]. Conventional in-situ and ex-situ processes for manufacturing the Al<sub>2</sub>O<sub>3</sub>-TiB<sub>2</sub> composite, are long and energy demanding processes which include milling [5–10], furnace [10–13] and microwave [14] sintering, densification processes [15–20], in situ and ex situ stir casting [21,22], welding and coating deposition methods [21,23–28]. There is a great interest in developing a rapid, low cost, and energy efficient process for manufacturing high purity Al<sub>2</sub>O<sub>3</sub>-TiB<sub>2</sub> composites for impact resistance applications, which exhibit superior microstructure, density and micro-hardness.

Self-propagating high temperature synthesis (SHS) describes highly exothermic chemical reactions whose reactants undergo rapid reaction, leading to temperature excursion not only above the melting points of the constituents but also of the products [1,29]. SHS is performed in a vacuum or inert atmosphere as the chemical reactions are of a redox nature in the absence of oxygen. The oxygen ion exchange occurring in situ results in an exothermic enthalpy yielding sintered and densified hard refractory materials [30]. The heat generated by the combustion develops temperatures within the range of 2000–5000K and

temperature rise rates of  $10^4$  to  $10^5$  K/s. The exothermicity of the chemical combustions has been exploited by various heating processes such as radio frequency, resistance furnace heating, and microwave sintering [11,31,32], for low-cost scalable manufacturing [1].

In the (Al + B<sub>2</sub>O<sub>3</sub>+TiO<sub>2</sub>) system, any deviation from the reaction stoichiometry resulted in partial reactions and the formation of Al-Ti and Al-B by-products in the case of excess aluminium, while for excess boric oxide, AlB<sub>2</sub>, AlBx, or (9Al<sub>2</sub>O<sub>3</sub>\*2B<sub>2</sub>O<sub>3</sub>) aluminoborate phases formed [10,33]. The presence of moisture in the starting mixture, primarily in the form of B<sub>2</sub>O<sub>3</sub>-H<sub>3</sub>BO<sub>3</sub>, triggered violent degassing phenomena during ignition, which generated porosity in the final composite matrix and resulted in the loss of stoichiometric boron [8,11,17,33,34].

The literature suggests different approaches to understanding the phase transformation in the starting mixture across the temperature range of 0–1673 K [7,34], with all studies concurring on the aluminium-mediated reduction of B<sub>2</sub>O<sub>3</sub> and TiO<sub>2</sub>, leading to the formation of TiB<sub>2</sub> from intermediate products. The reaction initiates with the melting of B<sub>2</sub>O<sub>3</sub> (723 K), while between 723 K and 933 K, the melted B<sub>2</sub>O<sub>3</sub> interacts with the 50 Å thick surface alumina layer coating the Al particles to form aluminoborate (Al<sub>2</sub>O<sub>3</sub>-B<sub>2</sub>O<sub>3</sub>) phases [33]. At 933 K, the molten aluminum actively contributes towards the reduction of the B<sub>2</sub>O<sub>3</sub> and TiO<sub>2</sub> reactants. The TiO<sub>2</sub> is reduced by Al at approximately 1133 K forming TiAl<sub>3</sub>, while the Al<sub>18</sub>B<sub>4</sub>O<sub>33</sub> and TiB<sub>2</sub> phases form at 1323 K and 1345 K, respectively [7,10,34]. The proposed reaction mechanisms in the literature regarding the in-situ fabrication of the Al<sub>2</sub>O<sub>3</sub>-TiB<sub>2</sub> composite are summarised in Supplementary S1.1. In addition to the by-product phases forementioned, the final composites might display Fe and Si contamination in the cases where milling and hot pressing are involved [5–10].

High temperature furnace sintering (1873 – 2123 K) and *in situ* hot pressing (1773 – 2223 K, 20–35 MPa, 8 – 120 min) produced the highest density Al<sub>2</sub>O<sub>3</sub>-TiB<sub>2</sub> composites, 90–99 % [15–20] in the literature. In-situ hot-pressing generated Al<sub>2</sub>O<sub>3</sub>-TiB<sub>2</sub> composites exhibiting TiB<sub>2</sub> aggregates at the central region, due to the high plasticity of the composites during SHS. Low temperature conventional sintering (1273 – 1473 K) produced composites of relative density ranging between 50 and 70 %, from reactants' green density of 55 – 80 % (cold pressed at 30 to 400 MPa) [10–13]. The TiO<sub>2</sub> particles defined the TiB<sub>2</sub> grain size [16, 21]. Any matrix porosity identified in the final product was attributed to intrinsic porosity in the TiB<sub>2</sub> grains due to the volume decrease (–28 %) recorded during the reaction and the porosity developed in the grain boundaries of TiB<sub>2</sub>. Additionally, degassing of impurities, water, H<sub>3</sub>BO<sub>3</sub> and B<sub>2</sub>O<sub>3</sub> [16,17,19] during ignition formed intra-granular voids and large voids at the central region of the samples [16,17]. Optimizing the manufacturing process through statistical design methods (ANOVA) and finite element analysis could improve the integrity of the produced composites [35].

The Vickers hardness of the Al<sub>2</sub>O<sub>3</sub>-TiB<sub>2</sub> composites in the literature, ranged from 16.1 to 26.3 GPa [10,11,15–20], while the fracture toughness laid between 4.2 and 6 MPa m<sup>1/2</sup> (Al<sub>2</sub>O<sub>3</sub>: 3.5 and TiB<sub>2</sub>: 6.2 MPa m<sup>1/2</sup> [36]). Additives such as B<sub>4</sub>C have been previously incorporated to the mixture to increase fracture toughness to 9.1 MPa m<sup>1/2</sup> [18–20]. Murno [36] reported TiB<sub>2</sub> compressive strength of 1.1 GPa and 1.8 GPa for densities of 3.8 g/cc and 4.51 g/cc respectively. Suleiman et al. identified that the effective strength of porous alumina (48 % to 28 %), varied from 17.63 to 137 MPa [37]. Shuai et al. identified a compressive strength of 142 MPa for alumina lattice structures synthesised through digital light processing (DLP) 3D printing technology and sintered to 95 % density [38].

Regarding the impact resistance performance of the Al<sub>2</sub>O<sub>3</sub>-TiB<sub>2</sub> composites, He and Wang [39], demonstrated that TiB<sub>2</sub> based ceramics exhibited improved ballistic resistance than high-strength steel samples. Shanazari et al. [40] and Chen et al. [41] also emphasised the bullet-proof performance and high strength-to-weight ratio of ceramic composites over rigid metals. Rozenberg et al. identified that the impact resistance performance of ceramic tiles increased linearly with the

improvement of the effective strength, which is the average of the static and dynamic compressive strengths divided by the density of the ceramic [42]. Zhai and Zhou [43] correlated the dependence of the ballistic performance of the  $\text{Al}_2\text{O}_3\text{-TiB}_2$  composites to their fracture toughness. Logan et al. [33] theorised that the impact performance of  $\text{Al}_2\text{O}_3\text{-TiB}_2$  composites was microstructure-dependent. However, Glide and Adams [44], on behalf of the US army, identified only a minor improvement in the ballistic performance of  $\text{Al}_2\text{O}_3\text{-TiB}_2$  composites presenting good dispersion of  $\text{TiB}_2$  particles in the  $\text{Al}_2\text{O}_3$  matrix, compared to composites displaying  $\text{Al}_2\text{O}_3$  agglomerates coated by  $\text{TiB}_2$  particles. On the contrary, the density of the composites contributed majorly to their impact resistance performance, which was also confirmed by Albafert et al. [45]. Zhai and Zhou [43] reported that the principle modes of failure, were the trans-granular and intergranular fracture of the  $\text{Al}_2\text{O}_3$  matrix, as a result of the distribution of the different phases, particle sizes and interfacial bonding. Weak interfacial bonding was the primary reason for failure, resulting from interfacial fracture through microcracks. Hertzian contact mechanics and impact mechanics enable the analysis of the stress, strain, and deformation that occur during the collision of objects. Hertzian contact mechanics are better suited for predicting surface deformations and stresses during impact, while impact mechanics provides a more comprehensive analysis of energy dissipation and fracture behaviour in bulk materials [42, 46–49]. Finite element analysis has been employed to predict stress evolution in nanocomposite joints, providing insight into failure mechanisms under load [50]. Parallel studies on the addition of nanoparticle to alloy matrices, have highlighted the potential of nanoscale reinforcements in modifying strength and mechanical response [51,52]. Increasing metal aluminium content in jute epoxy composites to 6 wt% significantly enhanced the failure load of the composites by 60 % [50].

Laser ignition chemical synthesis (LIChemS) is a novel technology demonstrated herein, that allows the rapid and energy-efficient synthesis of refractory materials suitable for impact resistance applications. LIChemS relies on the photoexcitation of chemically combustible mixtures, by accelerating the kinetics of thermodynamically favourable, highly exothermic, self-sustaining reactions [53]. The majority of the electromagnetic radiation is absorbed by the material and it is converted into the three different forms of heat, conduction, convection and radiation, while a small portion is scattered [54].

Literature regarding laser ignition synthesis primarily focuses on manufacturing alloys using high-power lasers (kW range). Some examples involve porous NiTiNol Shape Memory Alloy, Al–Ti–C system, Cu–Ti–Si system, TiC/Ni<sub>3</sub>Al composites,  $\text{Al}_2\text{O}_3\text{-Ti-C}$  system, joining Cf/Al composites and TiAl alloys, and porous high entropy alloy AlCrFeNiSi [55–60]. In contrast to conventional laser ignition synthesis, LIChemS relies on the keyhole welding phenomenon for generating plasma at the focal point. In laser beam welding, cavities “keyholes” form in the weld pool as a result of the recoil pressure from intense evaporation, due to high localised heating [61]. Keyholes can oscillate, collapse and deepen due to the interplay of i) vapour pressure, ii) surface tension, and iii) laser energy input [61]. High energy density is typically required to maintain the vapour capillary, with Cunningham et al. reporting 0.4 MW/cm<sup>2</sup> for Ti-6Al-4V samples [62], while Rai et al. reported 0.5 MW/cm<sup>2</sup> for laser welding of tantalum/Ti-6Al-4V/vanadium [63]. Vapour produced at the bottom or walls of the keyhole was partially trapped, increasing local pressure and temperature inside the keyhole, enhancing energy coupling, as the incident beam underwent multiple reflections off the keyhole walls [61,64]. LIChemS capitalises on this principle, forming a keyhole at the focal point, for relatively low laser intensities, taking advantage of the thermite exotherms [1,29], which lower the keyhole formation threshold. The trapped vapour can reach temperatures of several thousand Kelvin, due to i) light trapping in the keyhole and ii) exothermic reaction, resulting in the thermal ionisation of species such as Al and Ti for the current (Al-Ti-B-O) system, forming a partially ionised plasma plume [61]. For power densities above a certain threshold, “hot” plasma sustains the propagation of the reaction. The

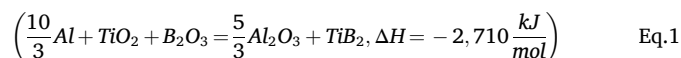
relaxation of hot plasma may involve propagation of energy via electrons/ions relaxing to the ground state by releasing heat in the form of radiation conduction and phonon conduction. Conductive heat transfer dominates in the micro-to sub nano second regime, whereas the convective heat transfer occurs much slower through molecular collision of fluid media on hot surfaces [54]. The molten pool sustaining the plasma plume exhibits Marangoni convection gradients ( $d\gamma/dT$ ), driven by surface tension stemming from intense temperature variations [65]. The gradients induce toroidal melt flows which align with the radial isotherms, advecting vapour bubbles formed by the oscillations taking place in the keyhole [61]. As the exothermic front decays, these bubbles are trapped in the solidifying melt forming porosity [61,65].

The state-of-the-art research discussing the manufacturing of  $\text{Al}_2\text{O}_3\text{-TiB}_2$  composites is mainly limited to conventional energy demanding processes. By contrast, in the proposed research, we aim to demonstrate a methodology for fabricating high purity, dense and hard  $\text{Al}_2\text{O}_3\text{-TiB}_2$  composites suitable for impact resistance application using lower laser intensity than reported in the literature. Unlike conventional thermite reactions, LIChemS reduced the processing time and energy consumption of the manufacturing process, while the underlying low-power and exotherm - driven mechanism of the technology, which leverages on the i) Keyhole formation, ii) Ionisation and iii) Marangoni convection, enabled the scalable manufacturing of bulk composites. The process is distinctive from conventional thermite and high power laser processes. We additionally propose an alternative reaction mechanism that accommodates the synthesis of the  $\text{Ti}_2\text{O}_3$  phase observed during composite characterisation. We present an analytical approach for correlating the ball dropping heights during impact testing to the defect sizes generated within the composites. A Newtonian cooling model correlated the temperature distribution following LIChemS to the generation of cracks within the composites. The developed methodology can be adjusted and implemented for manufacturing other energy demanding ceramic composites and metal-ceramic advanced materials.

## 2. Materials and methods

### 2.1. Experimental set-up

The  $\text{Al}_2\text{O}_3\text{-TiB}_2$  composites were manufactured in situ from the starting mixture of Al (200 mesh, 99.9 %),  $\text{TiO}_2$  (Titanium IV oxide, anatase powder, 99.8 %) and  $\text{B}_2\text{O}_3$  (99.98 %), purchased by sigma Aldrich, through a highly exothermic reaction, equation (1).



The reactant mixture ( $\text{Al-TiO}_2\text{-B}_2\text{O}_3$ ) was milled for 1 h at 30 Hz by RETSCH MM200 (steel vessel, alumina ball, ball – to – mass ratio of 9:5) and characterised by Daskalakis et al. [10] and the key findings are summarised in Table 1.

An overview of the i) experimental plan, ii) the methodology followed for the characterisation of materials and iii) the optimised manufacturing process that was developed in this research is summarised in the flow chart of Fig. 1.

The milled ( $\text{Al-TiO}_2\text{-B}_2\text{O}_3$ ) was heat treated (200–300 °C for 1 h), using a CARBOLITE Heating Laboratory Chamber Furnace. The heat-treated reactants were then pressed into cylindrical geometries of four

**Table 1**  
The milled reactant mixture of Al-TiO<sub>2</sub>-B<sub>2</sub>O<sub>3</sub>.

| Parameters                                                          | Specifications                                                          |
|---------------------------------------------------------------------|-------------------------------------------------------------------------|
| Composition (wt.%)                                                  | 0.375 Al – 0.334 TiO <sub>2</sub> – 0.291 B <sub>2</sub> O <sub>3</sub> |
| Milling Time (minutes)                                              | 60                                                                      |
| Al (d 0.1) (d 0.5) (d 0.9) (μm)                                     | 2.2   31.5   95.0                                                       |
| Particle Size TiO <sub>2</sub> & B <sub>2</sub> O <sub>3</sub> (nm) | Up to 600                                                               |
| Ignition Temperature (K)                                            | 1211                                                                    |

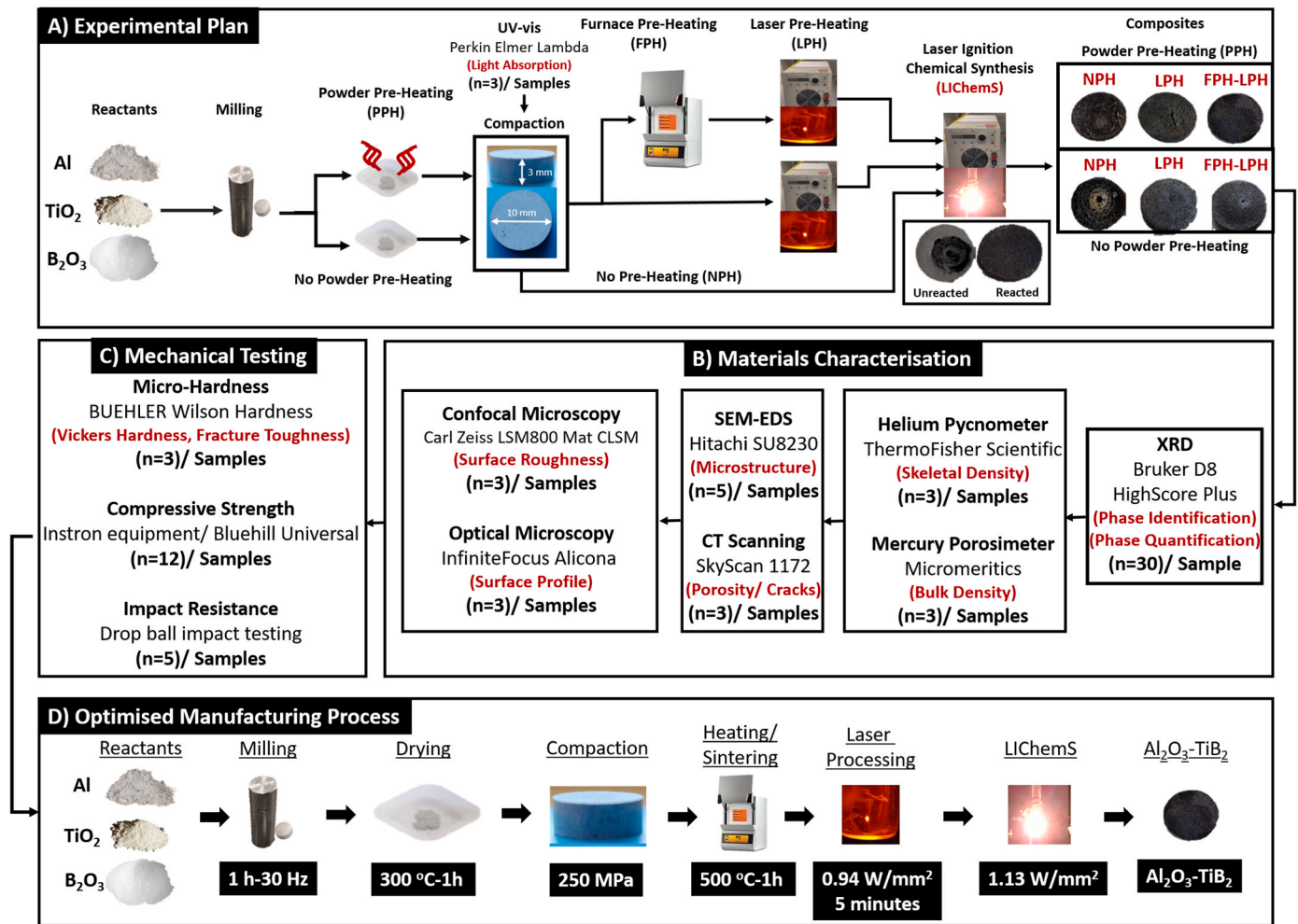


**Fig. 1.** An overview of the A) Experimental Plan, B) Materials characterisation, C) Mechanical testing and D) Optimised Manufacturing process explored in this research.

diameters: i) 5, ii) 10, iii) 13 and iv) 20 mm, by a hydraulic mechanical press, with the mass and thickness of the compacts ranging from 0.5 g to 3 g and 2 mm to 3 mm, respectively. The compacts were further heat treated (400–500 °C for 1 h) by the CARBOLITE furnace, before they were placed in a stainless steel sample holder inside the silica tube reactor.

The laser ignition experiments were conducted using an Amtron fibre optic integrated quasi-CW diode laser (976 nm), with a maximum output power of 30 W and an optical fibre core diameter of 200 μm. The laser beam was aligned and focused on the surface of the compact inside the silica tube reactor with the assistance of a laser card.

Laser Ignition Chemical Synthesis (LICHeMS) was performed inside a silica tube reactor (150 cm<sup>3</sup>), mounted on an optical bench. The reactor was purged with argon (Ar) gas at a flow rate of 1L/min to maintain inert conditions. Five volume exchanges were performed prior to LICHeMS for establishing a pure argon atmosphere. The fraction of air remaining in the reactor after (n) volume exchanges is given by equation (2).

$$C_{air} = C_o * e^{-n} \quad \text{Eq. 2}$$

Where ( $C_{air}$ ) is the concentration of air remaining, ( $C_o$ ) the starting concentration and (n) is the number of volume exchanges. The purging time required for achieving the volume exchanges was given by  $\left(t_{purge} = \frac{n * V}{V_{flow}}\right)$ , where (V) is the volume of the reactor and ( $V_{flow}$ ) is the argon flowrate.

The optimisation of LICHeMS included refining three parameters namely i) operating laser intensity to minimise energy consumption during synthesis, ii) drying and sintering conditions to ensure phase purity, structural integrity and improved mechanical properties in the composites, and iii) cold pressing parameters, as LICHeMS is a pressureless process. The optimised manufacturing methodology can find application in the synthesis of high-purity, dense Al<sub>2</sub>O<sub>3</sub>-TiB<sub>2</sub> bulk composites, and other ceramic composites.

## 2.2. Operating laser intensity

The minimum laser intensity for triggering LICHeMS in the (Al-TiO<sub>2</sub>-B<sub>2</sub>O<sub>3</sub>) system was identified through trial and error by adjusting the i) Laser power and ii) beam diameter at the focal point in accordance to equation (3) [66], where (I) is the laser intensity (W/m<sup>2</sup>), (P) the laser power (W) and ( $w_f$ ) the beam radius at the focal point (m).

$$I = \frac{P}{\pi * w_f^2} \quad \text{Eq. 3}$$

The fibre optic end (Focal distance 5 cm) of the Amtron laser was fixed on an optical bench using fibre mounts, in two pre-defined positions, Spot 1 and Spot 2, set to be 2.5 cm and 5 cm away respectively from the surface of the Al-TiO<sub>2</sub>-B<sub>2</sub>O<sub>3</sub> samples inside the silica tube reactor, Fig. 2. Ignitions from Spot 1 (2.5 cm) were performed bellow focus, while ignitions from Spot 2 (5 cm) were at focus, to examine variations in the efficiency of LICHeMS when performed bellow focus. A



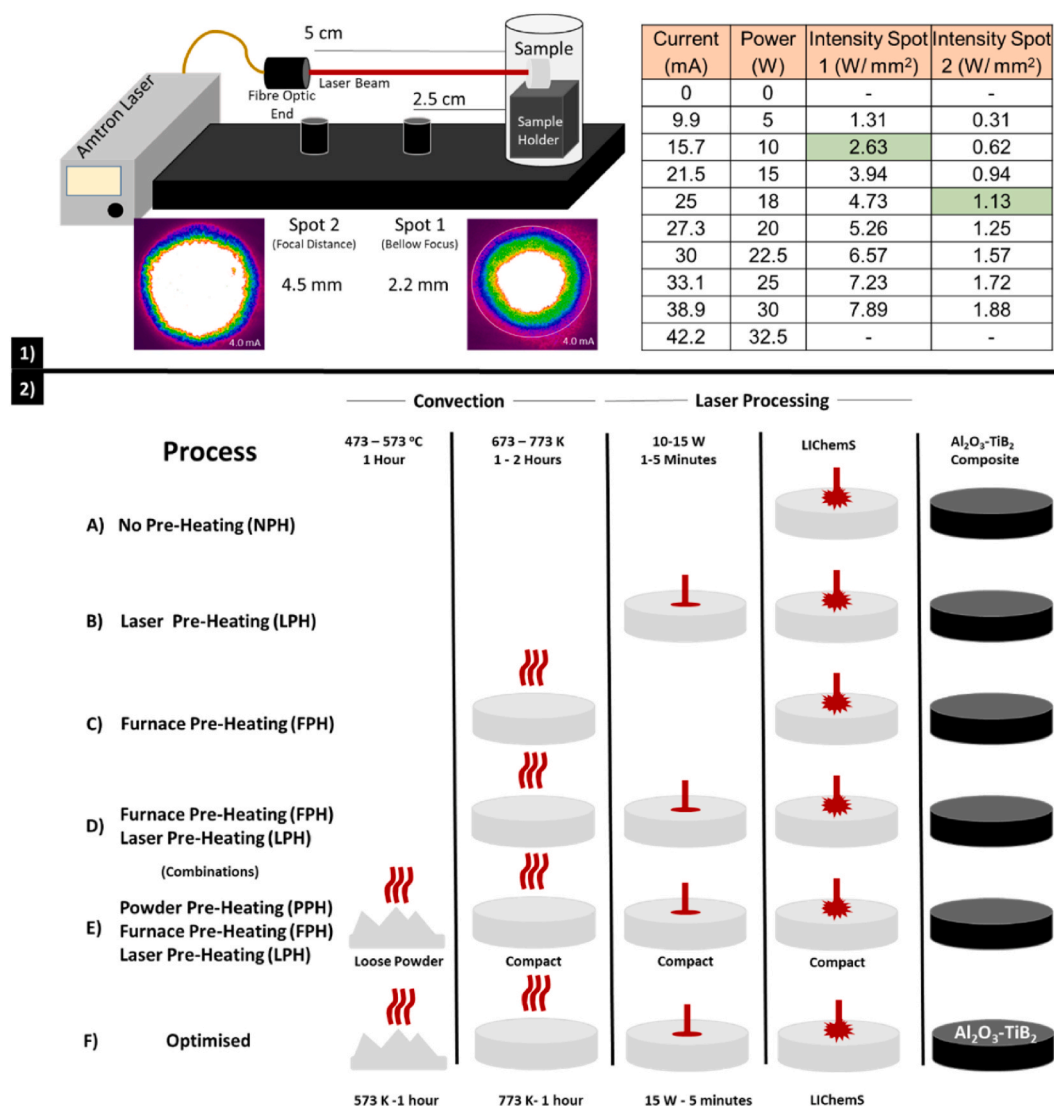


**Fig. 2.** 1) The experimental set up, beam diameters at the focal points Spot 1 (2.5 cm–2.2 mm) and Spot 2 (5 cm–4.5 mm). The minimum laser intensities at the focal point for triggering LiChemS from Spot 1 and Spot 2. 2) The processes of: A) No Pre-Heating (NPH), B) Laser Pre-Heating (LPH), C) Furnace Pre-Heating (FPH), D) Laser Pre-Heating (LPH) and Furnace Pre-Heating (FPH), E) Powder Pre-Heating (PPH). F) The optimum synthesis process.

Spiricon OPHIR photonics beam profiler measured the diameter of the beam at the focal points for both spots as 2.2 mm (Spot 1) and 4.5 mm (Spot 2), Fig. 2. The laser intensities at the focal points, from Spot 1 and Spot 2, were calculated using Equation (3). The minimum laser intensities required to trigger the reaction from Spot 1 and Spot 2 were 2.63 W/mm<sup>2</sup> and 1.13 W/mm<sup>2</sup>, respectively. The maximum laser intensity generated from spot 1 was 7.89 (W/mm<sup>2</sup>), compared to 1.88 (W/mm<sup>2</sup>) from spot 2, for a laser power of 30 W.

### 2.3. Drying and sintering parameters

Convection and CW laser processing, Figure 2-2, were employed for drying and sintering the (Al-TiO<sub>2</sub>-B<sub>2</sub>O<sub>3</sub>) reactants prior to LiChemS, Fig. 2. No Pre-Heating (NPH) was selected as the “control” processing technique, where the reactants were not subjected to heat treatment prior to LiChemS taking place. The sustained propagation of the reaction across the entire volume of the samples was feasible for laser intensities above 2.63 W/mm<sup>2</sup> (Spot 1) and 1.13 W/mm<sup>2</sup> (Spot 2 – Focal Point). The water absorbed by the reactants resulted in rapid degassing during LiChemS, with the produced composites demonstrating large cracks and advanced porosity. During Laser Pre-Heating (LPH), the compacted

reactants were dried and sintered using the Amtron laser before LiChemS. The samples were irradiated for 1 and 5 min using laser intensities of 0.62 and 0.94 W/mm<sup>2</sup> (10 and 15 W), as it was observed that both laser intensities enabled water removal from the sample at a reasonable rate. The ignition was then triggered, similarly to NPH processing, after re-adjusting the laser beam on the pre-heated surface of the samples. During Furnace Pre-Heating (FPH) convective drying and sintering was applied to the reactants, prior to LiChemS, with the assistance of a resistance furnace. The compacted reactants were heat treated at 673–773 K for 1 h, below and above the melting point of B<sub>2</sub>O<sub>3</sub> respectively. Combining FPH with 5 min of LPH at 0.94 (W/mm<sup>2</sup>) effectively removed the atmospheric water absorbed by the sample during the mounting process. Powder Pre-Heating (PPH) involved calcinating the loose powder mixture (Al-TiO<sub>2</sub>-B<sub>2</sub>O<sub>3</sub>) through convection (473–573 K, 1 h), prior to forming compacts. The optimised PPH technique provided crack free composites. The temperature selection was based on the DTA analysis by Daskalakis et. al. [8], where the endotherm for H<sub>3</sub>BO<sub>3</sub> decomposition was identified at 453 K. Daskalakis et. al identified that on average 0.07 g of water were absorbed per 1 g of (Al-TiO<sub>2</sub>-B<sub>2</sub>O<sub>3</sub>). Equation (5) provides the maximum mass of (Al-TiO<sub>2</sub>-B<sub>2</sub>O<sub>3</sub>) that can be adequately dried within 1 h of convective

drying.

$$m_w = \frac{t_{dry} * Q_{input\ rate}^*}{0.075 * \lambda w} \quad \text{Eq 5}$$

Where ( $t_{dry}$ ) is the duration required for evaporating the absorbed water, ( $m_w$ ) is the mass of water and ( $\lambda w$ ) is the latent heat of vaporization of water (2260 kJ/kg).

The optimum process for manufacturing the  $\text{Al}_2\text{O}_3\text{-TiB}_2$  composites involved: i) milling the reactants for 1 h at 30 Hz (Daskalakis et al. [10]), ii) calcinating the mixture at 573 K for 1 h, iii) compacting the loose reactants at 250 MPa, iv) perform convective sintering of the compact at 773 K for 1 h and v) pre-heating the compacts for 5 min at 0.94 W/mm<sup>2</sup> and vi) performing LiChemS, Fig. 1.

#### 2.4. Cold pressing conditions

Since LiChemS is a pressure-less processing method, a range of pressures (74–1000 MPa) was tested for forming dense  $\text{Al}_2\text{O}_3\text{-TiB}_2$  composites, with examples presented in the **Supplementary S2.1**. The theoretical densities of the reactants and products were calculated as  $2.94 \left(\frac{\text{g}}{\text{cm}^3}\right)$  and  $4.16 \left(\frac{\text{g}}{\text{cm}^3}\right)$  respectively. The relative density of reactants pressed at 250 MPa was 69.13 %.

#### 2.5. Materials characterisation

Phase identification was performed by X-Ray diffraction (XRD) (Bruker D8) with monochromatic  $\text{CuK}\alpha$  radiation ( $\lambda = 0.154$  nm) and a  $2\theta$  range of  $10\text{--}80^\circ$ . Phase quantification, through Retvield analysis was performed with the assistance of High Score Plus software. The micro-structural characterisation of the samples was carried out by Scanning Electron Microscopy (SEM) and Energy Dispersive X-Ray Spectroscopy (EDS) (Hitachi SU8230, TM3030PLUSUSER) operating at 2–20 kV in backscattered and secondary electron imaging modes. The samples were loaded onto SEM metal stubs, then carbon-coated (10 nm) and painted to prevent charging from occurring. For skeletal density measurements, a ThermoFisher Scientific Helium-Pycnomatic was used at 20 °C, for 20 cc sample volume, while the average of 10 runs was collected. A Micromeritics mercury porosimeter was used to determine the bulk density of the composite. It operated at a vacuum, with a maximum pressure of 413 MPa applied. A SkyScan 1172 micro-CT scanner (100 kV, 100  $\mu\text{A}$ , Al + Cu filter) with a  $13.65\ \mu\text{m}$  voxel size (2x2 binning, 8.99  $\mu\text{m}$  camera pixel) was used to identify the porosity in the composites, with the assistance of Image J thresholding. The PerkinElmer Lambda 905 UV–visible–NIR spectrometer recorded the optical reflectance of the reactive mixture, at a wavelength range of 200 – 1400 nm. The surface roughness of the  $\text{Al}_2\text{O}_3\text{-TiB}_2$  composites was evaluated using a confocal laser-scanning microscope (Carl Zeiss LSM800 Mat CLSM), while the profile of the ablated crater was observed using an InfiniteFocus Alicona profilometer. The characterisation equipment are available in the **Supplementary S2.2**.

#### 2.6. Mechanical testing

The Vickers Hardness of the composites was examined by a BUEHLER Wilson Hardness equipment, with available loads of 0.1, 0.2, 0.3, 0.5, 1 and 2 kg. The diamond micro-intender was pressed against the sample for 10 s. The fracture toughness of the composite was calculated from the crack propagating from the diagonals of the indentation performed by the BUEHLER Wilson Hardness equipment.

The compressive strength of the optimum NPH, LPH, FPH-LPH and PPH-FPH-LPH composites ( $n = 12$ ) was compared to the compressive strength of synthesised  $\text{Al}_2\text{O}_3$  pellets ( $d_{0.5} = 50\ \mu\text{m}$ , 250 MPa for 5 min, sintered at 1300 °C for 10 h), ISO standard 17162:2014, performed at ambient temperature ( $23 \pm 2$  °C) and relative humidity ( $50 \pm 10$  %).

Both surfaces of each sample were levelled using coarse-grit sandpaper (P400). The compressive strength tests were performed using an Instron equipment and the data was recorded by the Bluehill Universal software. The data collected was converted into strain graph using equations ( $\sigma = \frac{F}{A}$ ) and ( $\epsilon = \frac{\Delta L}{L_0}$ ), where ( $\sigma$ ) is the compressive stress (Pa), ( $F$ ) is the applied force (Newtons) and ( $A$ ) is the area of the sample ( $\text{m}^2$ ), ( $\epsilon$ ) is the strain, ( $L$ ) is the displacement and ( $L_0$ ) the original Length. The cross-head speed was set to 0.5 mm/s, and the maximum allowable displacement before stopping the measurement was set according to the thickness of sample. For the NPH samples with an average thickness of 5 mm after grinding, the displacement was set to (4 mm). Similarly for the LPH ( $W = 4$  mm), FPH-LPH ( $W = 3.4$  mm) and PPH-FPH-LPH ( $W = 2.8$  mm) samples, the allowable displacement before stopping the measurements were set to 3, 2.5 and 2.5 mm respectively. The strain rate was calculated as 0.16 (1/s) according to ( $\text{Strain Rate} = \frac{\text{Compressive Speed}}{\text{Thickness of Sample}}$ ).

The impact resistance performance of the PPH-FPH-LPH composites was examined using drop ball impact testing. Stainless steel balls of 14, 66 and 178 g with diameters of 15, 25.4 and 35 mm respectively, were dropped on the synthesised composites from predefined heights, with the assistance of an electromagnet. The samples were placed on stainless steel slabs 10 cm thick, fixed to an optical bench. An analytical model integrating Hertzian contact mechanics [42,46–48] and impact mechanics [49] was developed to estimate the critical drop height from which the stainless-steel balls will not fracture the  $\text{Al}_2\text{O}_3\text{-TiB}_2$  composites. The plots correlating the critical drop heights to the defect size in the composites are included in the results section.

The contact radius and contact area between the sphere balls and the surface of the composites were calculated from equations (7) and (8).

$$a_c = \left( \frac{3 F R s s b}{4 E^*} \right)^{\frac{1}{3}} \quad \text{Eq. 7}$$

Where ( $R$ ) is the radius of the stainless steel ball, ( $F$ ) is the force and ( $E^*$ ) is the effective elastic modulus. Then, the contact area during impact was calculated using Equation (8).

$$A = \pi r^2 = 2.6 \left( \frac{F R s s b}{E^*} \right)^{\frac{2}{3}} \quad \text{Eq.8}$$

The effective elastic modulus was calculated by equation (9), where ( $\nu$ ) is the Poisson Ratio of the stainless steel balls is defined by.

$$\frac{1}{E^*} = \frac{1 - \nu_{ball}^2}{E_{Ball}} + \frac{1 - \nu_{composite}^2}{E_{composite}} \quad \text{Eq. 9}$$

For a spherical object impacting a flat surface, the maximum contact stress generated at impact was calculated using equation (10).

$$\sigma_{max} p_0 = \frac{3 F}{2 \pi a^2} \quad \text{Eq. 10}$$

To calculate the minimum height required to prevent fracture of the surface of  $\text{Al}_2\text{O}_3\text{-TiB}_2$  composites, the maximum contact stress ( $\sigma_C$ ) induced by the impact was calculated to be less than or equal to the critical stress ( $\sigma_{max}$ ) of the material, as shown in equation (11).

$$\sigma_{max}(p_0) \leq \sigma_C \quad \text{Eq. 11}$$

The critical stress of the  $\text{Al}_2\text{O}_3\text{-TiB}_2$  composite was calculated based on equation (12), where ( $K_{IC}$ ) is the fracture toughness of the  $\text{Al}_2\text{O}_3\text{-TiB}_2$  composite and ( $c$ ) is the defect size.

$$\sigma_{crit} = \frac{K_{IC}}{\sqrt{\pi a_d}} \quad \text{Eq.12}$$

Then the kinetic energy at the point of impact was provided by equation (13).

$$E_k = \frac{1}{2} m v^2 = m g h \quad \text{Eq.13}$$

The force at impact that is deforming the material is provided by equation (14).

$$F = \frac{\Delta p}{\Delta t} = \frac{E_{kin}}{d} = \frac{mgh}{d} \quad \text{Eq.14}$$

Substituting equations (7), (12) and (13) in equation (10) for ( $h_{sf}$ ), we can identify the height from which each ball can initiate fracture on the surface of the  $\text{Al}_2\text{O}_3$ - $\text{TiB}_2$  composites, equation (15). The analytical calculations are included in the **Supplementary S2.3**.

$$h_{sf} = \left( \frac{K_{IC} d^{\frac{1}{3}} 2\pi \left( \frac{3R}{4E} \right)^{\frac{2}{3}}}{3 \sqrt{\pi a} (mg)^{\frac{1}{3}}} \right)^3 \quad \text{Eq.15}$$

Assuming that the stress is proportional to strain during impact and is uniformly spreading throughout the volume of the material without exceeding the elastic limit of the material, then the energy required for fracturing the bulk  $\text{Al}_2\text{O}_3$ - $\text{TiB}_2$  composite was provided by Equation (16) [49], where ( $U$ ) is the energy at impact, ( $\sigma_{crit}$ ), ( $V$ ) and ( $E$ ) are the critical stress, volume and Young's Modulus of the composite.

$$U = \frac{1}{2} \frac{\sigma_{crit}^2 V}{E} \quad \text{Eq.16}$$

For ( $U = mgh$ ) at the point of impact, the minimum height for fracturing the bulk  $\text{Al}_2\text{O}_3$ - $\text{TiB}_2$  composite was calculated based on equation (17). The analytical calculations are included in the **Supplementary S2.3**. The theoretical and experimental heights are summarised in Table 2 [2,3].

$$h_{bf} = \frac{1}{2} \frac{\sigma_{crit}^2 V}{mgE} \quad \text{Eq.17}$$

### 3. Results

#### 3.1. UV-vis analysis

The absorption coefficient of the ( $\text{Al-TiO}_2$ - $\text{B}_2\text{O}_3$ ) mixture was measured before performing LiChemS. Fig. 3 demonstrates the absorbance and reflectance spectra of the reactants (3 mm thickness and 10 mm diameter). The reflectance of ( $\text{Al-TiO}_2$ - $\text{B}_2\text{O}_3$ ) at 976 nm wavelength was measured as 57 %, while the transmittance was assumed negligible. The absorbance was calculated using equation (18) [67].

$$1 = A + R + T \quad \text{Eq. 18}$$

The absorption coefficient was calculated as 33 %, equation (19) [67]:

$$a = 2.303 \frac{A}{d} = 33\% \quad \text{Eq. 19}$$

#### 3.2. Laser ignition chemical synthesis (LiChemS)

Laser ignition chemical synthesis is displayed in Fig. 4-A i). The highly exothermic reaction was triggered at the focal point within the

**Table 2**

The maximum heights for dropping the stainless steel balls without fracturing the  $\text{Al}_2\text{O}_3$ - $\text{TiB}_2$  composites were calculated using Hertzian contact mechanics.

| Ball Mass (g) | Ball Diameter (mm) | Contact Area ( $\text{m}^2$ ) | Theoretical Height for Surface Fracture (m) | Theoretical Height for Bulk Fracture (m) | Experimental Heights (m) |
|---------------|--------------------|-------------------------------|---------------------------------------------|------------------------------------------|--------------------------|
| 14            | 15                 | $9.1 \times 10^{-10}$         | 0.03                                        | 0.87                                     | 0.65                     |
| 66            | 25.4               | $3.63 \times 10^{-9}$         | 0.019                                       | 0.23                                     | 0.2                      |
| 178           | 35                 | $7.8 \times 10^{-9}$          | 0.013                                       | 0.08                                     | 0.08                     |

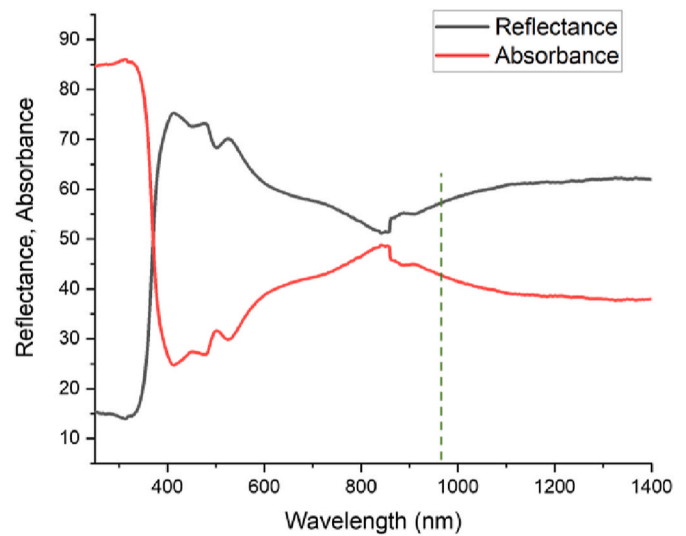


**Fig. 3.** The UV-vis analysis of the  $\text{Al-TiO}_2$ - $\text{B}_2\text{O}_3$  mixture was used to identify the reflectance and absorbance of the reactants at a wavelength of 976 nm.

first second of the interaction between the laser beam and the sample, following the reduction of  $\text{B}_2\text{O}_3$  and  $\text{TiO}_2$  by aluminium. In Fig. 4-A ii) the heat wave propagated across the ( $D = 10$  mm, Thickness = 3 mm) compact within 3 s, which emphasises on the rapid heating rates of (LiChemS). An intense outgassing phenomenon was observed, between the third and fifth seconds, after which the thermal decay was initiated. In Fig. 4-A iii), (6<sup>th</sup> and 13<sup>th</sup>) seconds, the temperature was estimated to drop below 673 K due to rapid cooling, as measured with the assistance of a thermocouple. The adiabatic temperature of the system was calculated as 2643 K (Supplementary S3.1), equation (20) [68].

$$Q = -\Delta H_{298} = \int_{298}^{T_{ad}} \Sigma C_p(\text{Products}) dT \quad \text{Eq. 20}$$

A Newtonian cooling model was employed to identify the temperature distribution across the sample during cooling, for correlating it to potential crack generation within the ceramic matrix after LiChemS was performed. The model accounted for the adiabatic temperature rise due to the exothermic reaction, as shown in equation (21) [69]. Where ( $T_{amb}$ ) is the room temperature, ( $T_{ad}$ ) is the adiabatic temperature, ( $h$ ) is the convective heat transfer coefficient, ( $A_s$ ) is the surface area of the disk, ( $\rho$ ) is the density, ( $C_p$ ) is the specific heat capacity ( $\text{J/gK}$ ) and ( $V$ ) the volume of the sample.

$$T(t) = T_{amb} + (T_{ad} - T_{amb}) \exp\left(-\frac{hA_s}{\rho CV} t\right) \quad \text{Eq.21}$$

The heat transfer coefficients of the composite was calculated as  $13 \text{ W/m}^2\text{K}$  from equation (22) (Supplementary S3.2) [70,71], where ( $k_f$ ) is the thermal conductivity of argon gas, ( $g$ ) is acceleration due to gravity, ( $\beta$ ) coefficient of thermal expansion of argon ( $2 \times 10^{-3} \text{ 1/K}$ ), ( $\Delta T$ ) is the temperature difference, ( $L$ ) is the length of the composite and ( $\nu$ ) kinematic viscosity of argon, ( $\rho_f$ ) is the density of argon, ( $\mu$ ) is the dynamic viscosity of argon.

$$h = \frac{k_f}{L} \left[ 2 + \left( 0.589 \left( \frac{g \beta \Delta T L^3 C_p \mu}{k_f \nu^2} \right)^{\frac{1}{4}} \left( 1 + \frac{0.469 k_f}{cp \mu} \right)^{\frac{9}{16}} \right)^{\frac{4}{5}} \right] \quad \text{Eq. 22}$$

As the surface of the  $\text{Al}_2\text{O}_3$ - $\text{TiB}_2$  composite cooled faster than the centre, the differential temperature between the outer layers of the composite and the centre created strain at the centre [69]. The relatively ductile state of the high-temperature centre allowed the partial accommodation of the strain. However, when the centre cooled, the rigid state of the outer layers did not accommodate the strain, resulting in the

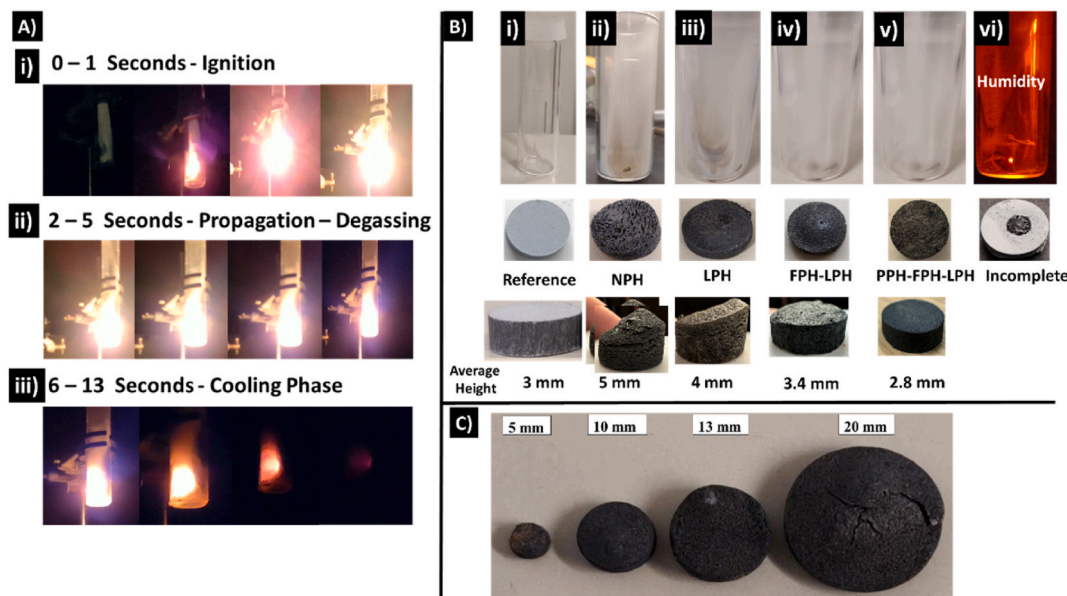


**Fig. 4.** A i) LiChemS onset on  $\text{Al-TiO}_2\text{-B}_2\text{O}_3$ . A ii) Propagation of LiChemS (3 s), water and impurities degassing. A iii) Cooling phase (9 s), after which temperature drops below 473 K. B) Exhibits the silica tube reactor and the porosity of the composites during 1) Reference, 2) NPH. 3) LPH. 4) FPH-LPH. 5) LPH processing. C) The  $\text{Al}_2\text{O}_3\text{-TiB}_2$  composites with diameters of 5, 10, 13 and 20 mm.

generation of tangential stress, which exceeded the critical stress of the composite and therefore generated cracks in the structure [69]. Equation (23) provides the temperature variation within the sample ( $D = 10$  mm, thickness = 3 mm) over time, assuming high thermal conductivity for instantaneous heat distribution within the material.

$$T(t) = 298 + (2345)\exp(-0.18t) \quad \text{Eq. 23}$$

The thermal stresses generated within the structure can be described by equation (24) [72], where ( $\alpha_{th}$ ) is the thermal expansion coefficient, ( $E$ ) is the Young's Modulus and ( $\Delta T$ ) is the temperature difference [69].

$$\sigma_{th} = E \alpha_{th} \Delta T \quad \text{Eq. 24}$$

For a thermal expansion coefficient ( $\text{Al}_2\text{O}_3\text{-TiB}_2$  composite) of ( $8.2 \times 10^{-6} \text{ K}^{-1}$ ), Young's Modulus of (400 GPa) and an average fracture strength of 250 MPa, the minimum differential temperature of 349 K can result in the formation of cracks within the matrix of the composite (Supplementary S3.3).

The activation energy of LiChemS was calculated as 11.6 kJ/mol using the Kissinger equation (25) [73], where ( $\beta$ ) is the heating rate of the material, ( $T_p$ ) is the ignition temperature and ( $R$ ) is the gas constant (Supplementary S3.4). The activation energy for conventional convective heating at 10 C/min was calculated as 119 kJ/mol.

$$E = -R \frac{d \ln \left( \frac{\beta}{T_p^2} \right)}{dT_p^{-1}} \quad \text{Eq. 25}$$

The heating rate during laser processing was provided by equation (26), where  $P$  is the laser power (W), ( $\alpha$ ) is the absorption coefficient, ( $m$ ), ( $C_p$ ) and ( $A$ ) are the mass, specific heat capacity and area of the reactants [73].

$$\beta = \frac{P \alpha}{m C_p A} \quad \text{Eq. 26}$$

In Fig. 4-B, the  $\text{Al}_2\text{O}_3\text{-TiB}_2$  composites and the tube reactor after each of the processing methods are presented. The reference tube and reactants are displayed in Fig. 4-B i). In Fig. 4-B ii) the NPH composite presented a highly porous structure due to the rapid degassing of water,  $\text{B}_2\text{O}_3$  and  $\text{H}_3\text{BO}_3$  during LiChemS. The LPH composite in Fig. 4-B iii) exhibited

improved structural integrity and the tube was significantly less polluted. Fig. 4-B vi) displays the laser-induced drying and sintering process, where the water removed from the reactants was deposited on the inner walls of the tube. In Fig. 4-B iv) and v) the FPH-LPH and PPH-FPH-LPH composites presented low porosity, while the mild severity ignitions minimised the degassing phenomenon. Fig. 4-C, displays  $\text{Al}_2\text{O}_3\text{-TiB}_2$  composites of 4 different diameters 5, 10, 13 and 20 mm. The ignition propagated across the chemically combustible mixture for the same laser intensity ( $1.13 \text{ W/mm}^2$ ), emphasising on the scalability potential of the process. A comparison between the laser intensities used across the literature for performing laser ignition synthesis are displayed in Table 5.

### 3.3. Compositional analysis

Fig. 5 exhibits the XRD plots of the composites manufactured through the optimised processing techniques of NPH (18 W, 5 min), LPH (15 W, 5 min), FPH (773 K–2 h, 15 W–5 min) and PPH - FPH - LPH (573 K–1 h, 773 K–1 h, 15 W–5 min). The X-ray diffractograms of Fig. 5 indicate that the yield of the  $\text{Al}_2\text{O}_3$  and  $\text{TiB}_2$  phases improved proportionally to the effectiveness of each processing method in drying and sintering the reactants before LiChemS [10]. The Al-B-O phases, previously observed during furnace processing [10], were not present in the composites, however the  $\text{TiAl}_3$  phase was detected in the NPH-composites, due to  $\text{H}_3\text{BO}_3$  being present in the reactants during LiChemS [78]. The 100 % peaks of  $\text{Al}_2\text{O}_3$ ,  $\text{TiB}_2$  were present in all of the diffractograms [11,69,78].

Compositional analysis commenced in the NPH composites from Spot 1 (2.5 cm). NPH primarily relied on the exothermicity of the chemical reaction rather than the laser processing aspect of LiChemS. Four laser intensities i)  $3.94 \text{ W/mm}^2$  (15 W), ii)  $5.26 \text{ W/mm}^2$  (20 W), iii)  $7.23 \text{ W/mm}^2$  (25 W) and iv)  $7.89 \text{ W/mm}^2$  (30 W) were tested. All composites presented the same four phases of  $\text{Al}_2\text{O}_3$ ,  $\text{TiB}_2$ ,  $\text{Ti}_2\text{O}_3$  and  $\text{TiAl}_3$  [78] (Supplementary S3.5). The by-product phases reduced proportionally to the laser intensity decrease LiChemS ( $N = 30$ ). NPH performed from the focal distance (Spot 2) produced composites exhibiting three phases of  $\text{Al}_2\text{O}_3$ ,  $\text{TiB}_2$  and  $\text{Ti}_2\text{O}_3$ , for laser intensities of  $1.13 \text{ W/mm}^2$  (18 W),  $1.72 \text{ W/mm}^2$  (25 W) and  $1.88 \text{ W/mm}^2$  (30 W), ( $N = 30$ ) (Supplementary S3.5). LiChemS from the focal distance provided greater purity composites for all processing techniques.



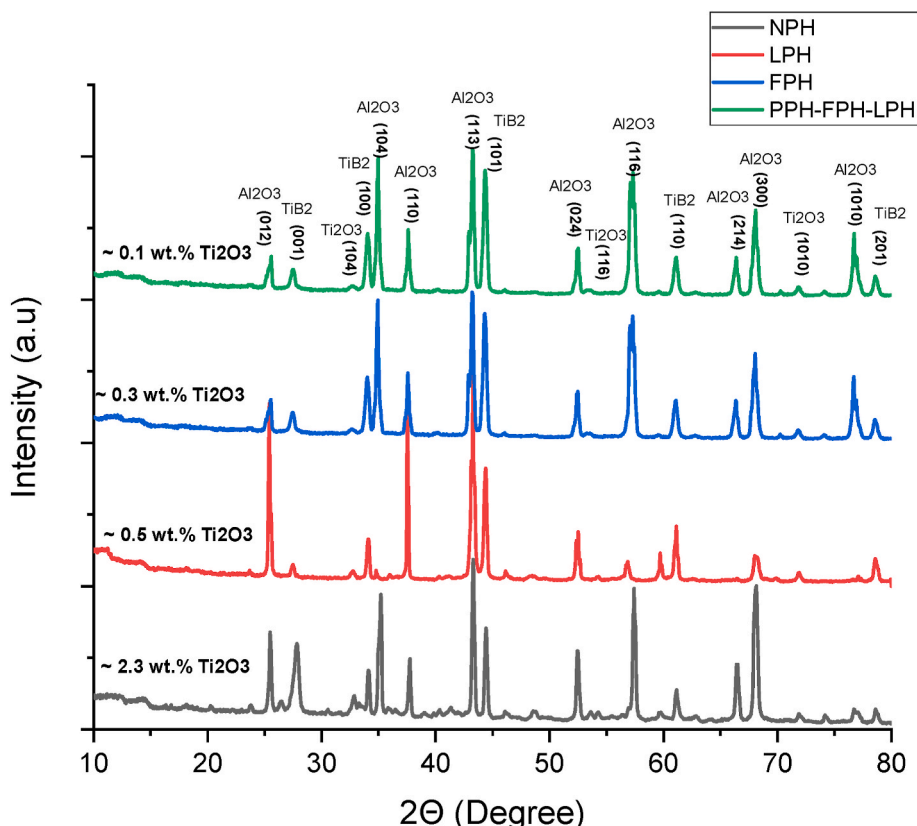


Fig. 5. The XRD plots of the composites deriving from the optimised NPH (18 W), LPH (15 W, 5 min), FPH (773 K–2 h, 15 W–5 min) and PPH (573 K–1 h, 773 K–1 h, 15 W–5 min) techniques.

The LPH composites exhibited three phases of  $\text{Al}_2\text{O}_3$ ,  $\text{TiB}_2$  and  $\text{Ti}_2\text{O}_3$  **Supplementary S3.6**. The wt.% of  $\text{Ti}_2\text{O}_3$  averaged 1.1 wt%, compared to the 2.6 wt% of the NPH composites ( $N = 30$ ). Five minutes of LPH was more efficient in: i) dissolving the intrinsic crystallised  $\text{H}_3\text{BO}_3$  from the  $\text{H}_3\text{BO}_3\text{-B}_2\text{O}_3$  mixture ii) drying the reactants, compared to 1 min, for each of the laser intensities tested. The highest-purity LPH composite (0.5 wt%  $\text{Ti}_2\text{O}_3$ ) was obtained when using  $0.94 \text{ W/mm}^2$  for 5 min.

FPH-LPH produced composites of higher purity ( $N = 30$ ), resembling the theoretical stoichiometry (0.65  $\text{Al}_2\text{O}_3$  and 0.35  $\text{TiB}_2$ ), however the  $\text{Ti}_2\text{O}_3$  was still present in the composites **Supplementary S3.7**. The average wt.% of  $\text{Ti}_2\text{O}_3$  reduced to 0.3 wt% for FPH-LPH samples (773 K–1 h,  $0.94 \text{ W/mm}^2$ –5 min). The yield of  $\text{TiB}_2$  was improved for FPH above the melting point of  $\text{B}_2\text{O}_3$  at 773 K.

The diffractograms of (PPH–NPH), (PPH–LPH) and (PPH–FPH-LPH) composites are available in the **Supplementary S3.8**. The PPH-NPH ( $1.25 \text{ W/mm}^2$ –20 W) composites contained 1.8 wt%  $\text{Ti}_2\text{O}_3$  compared to NPH composites (2.6 wt%). For PPH–LPH ( $0.94 \text{ W/mm}^2$ –15 W), the average concentration of the  $\text{Ti}_2\text{O}_3$  phase reduced to 0.6 wt% from the previous 1.1 wt% (LPH composites). PPH-FPH-LPH processing (573 K, 1h–773 K, 1h–15 W, 5 min) produced composites of high purity  $\text{Al}_2\text{O}_3$ – $\text{TiB}_2$  (~0.1 wt%  $\text{Ti}_2\text{O}_3$ ). The reaction mechanisms abiding by the results of the compositional analysis presented herein, differ from the literature [5–7,22,34], and are included in the **Discussion** section.

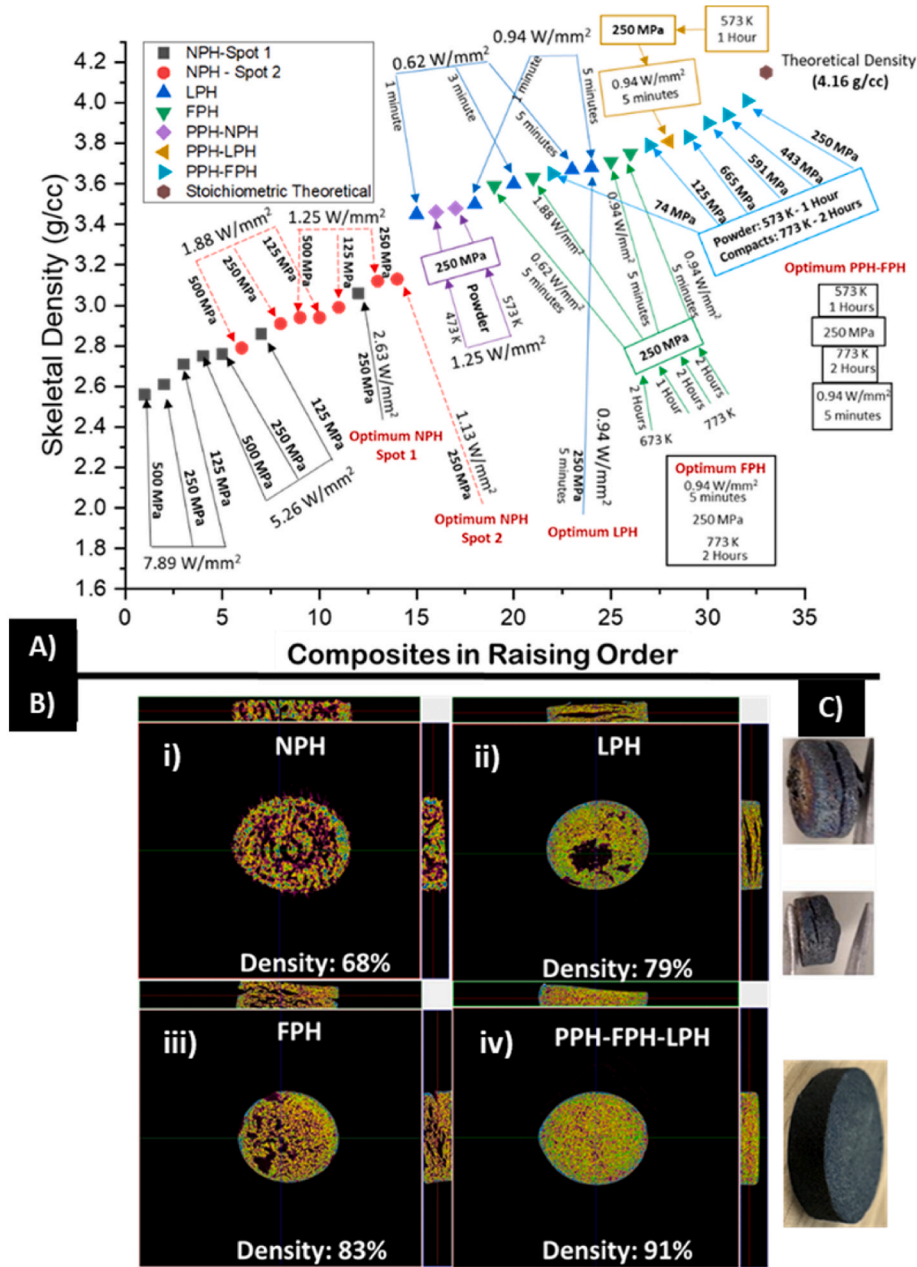
### 3.4. Density and structure

Fig. 6A demonstrates the skeletal densities of LiChemS composites, **Supplementary S3.9**. NPH-composites exhibited the lowest skeletal densities among all LiChemS composites, featuring highly porous structures attributed to the volume reduction and the rapid degassing during LiChemS, previously seen in furnace and in-situ hot pressing [11, 17]. The degassing phenomenon was amplified for high laser intensities

[55]. Still LiChemS composites presented greater skeletal density than furnace synthesised composites [10,11]. The compaction pressure of 250 MPa provided NPH composites with the highest skeletal density, compared to 125 MPa and 500 MPa, for laser intensities of i)  $5.26 \text{ W/mm}^2$  and ii)  $7.89 \text{ W/mm}^2$  (Spot 1) and i)  $1.25 \text{ W/mm}^2$  and ii)  $1.88 \text{ W/mm}^2$  (Spot 2). The greatest skeletal density (3.11 g/cc, 74.76 %) for the NPH-composites was provided for compaction at 250 MPa and LiChemS at  $1.25 \text{ W/mm}^2$ .

The optimum LPH composites ( $0.94 \text{ W/mm}^2$ –5 min) presented 0.44 g/cc skeletal density improvement (3.65 g/cc–88.59 %) from the optimum NPH-composites. FPH at (773 K) provided composites with a higher skeletal density than FPH at (673 K) possibly due to the improved spread ability of  $\text{B}_2\text{O}_3$  [17]. FPH-NPH composites displayed greater skeletal density than NPH composites by (0.6 g/cc). The skeletal density of the optimum FPH-LPH composites (3.74 g/cc, 90.29 %) was greater by (0.09 g/cc) compared to LPH composites. PPH-NPH composites (573 K–1 h, 18W) and PPH-LPH composites (473 K–1 h, 18 W) provided skeletal densities of 3.48 (g/cc) and 3.46 (g/cc) respectively. The optimum PPH-LPH composites and PPH-FPH-LPH composites displayed skeletal densities of 3.81 g/cc and 4.01 g/cc (96.62 %) respectively, which were the highest recorded. The 250 MPa pressure provided the highest skeletal density composites during PPH processing.

LPH and FPH techniques were prone to generating macro-cracks in the matrices of the composites, primarily due to the evaporation of water, previously seen in the literature during furnace drying [10,17], which compromised both the skeletal and bulk densities of the final products Fig. 6B and C. The structure and bulk densities of the NPH, LPH, FPH and PPH-FPH-LPH composites was observed using CT scanning and their density was identified using Image J thresholding, Fig. 6-B. CT scanning measured the X-ray attenuation through the high density phases  $\text{Al}_2\text{O}_3$  and  $\text{TiB}_2$ , governed by Beer's Law ( $I = I_0 e^{-\mu x}$ ), enabling detection of low-density pores and cracks [79]. The



**Fig. 6.** 1) The skeletal densities of the NPH, LPH, FPH and PPH derived  $\text{Al}_2\text{O}_3\text{-TiB}_2$  composites. 2) The densities of NPH, LPH, FPH and PPH-FPH-LPH composites as identified by CT-scanning. 3) Macro-cracks and macroscopic defects that form on the compacts during LPH and FPH processing, attributed to water evaporation.

PPH-FPH-LPH composites (91.4 %) presented ~38 % greater relative density than the NPH composites (68 %). The NPH-composites demonstrated uniform distribution of porosity as a result of water and  $\text{B}_2\text{O}_3$

**Table 3**  
Bulk density measurements performed by mercury porosimetry for: i) NPH), ii) LPH, iii) FPH, iv) FPH-LPH) and v) PPH-FPH-LPH.

| Composites  | Bulk Density including Macro-Cracks | Porosity % including Macro-Cracks | Bulk Density excluding Macro-Cracks | Porosity % excluding Macro-Cracks |
|-------------|-------------------------------------|-----------------------------------|-------------------------------------|-----------------------------------|
| NPH         | 3.06                                | 26.3                              | 3.24                                | 24.3                              |
| LPH         | 2.88                                | 30.5                              | 3.45                                | 16.2                              |
| FPH         | 2.52                                | 37.6                              | 3.59                                | 13.4                              |
| FPH-LPH     | 2.32                                | 41.6                              | 3.62                                | 12.8                              |
| PPH-FPH-LPH | 3.79                                | 8.3                               | 3.83                                | 8.0                               |

evaporation across the entire volume of the sample. The bulk density of the NPH, LPH, FPH, FPH-LPH and PPH-FPH-LPH composites was also measured using mercury porosimetry, Table 3. NPH and PPH-FPH-LPH composites exhibited the same bulk densities when accounting macro-cracks induced during cold pressing and drying. However the LPH, FPH and FPH-LPH composites displayed different bulk and matrix densities. The best relative bulk density was measured for the PPH-FPH-LPH samples, 3.83 (g/cc), 92 %.

### 3.5. Surface profile analysis

The surface profile of the composites was observed using scanning electron, optical and confocal microscopies. In Fig. 7A and B, NPH composites demonstrated surface roughness of 57.9  $\mu\text{m}$ , featuring large cracks and interconnected porosity, result of the degassing of water and impurities during LiChemS. The porosity and surface roughness of the

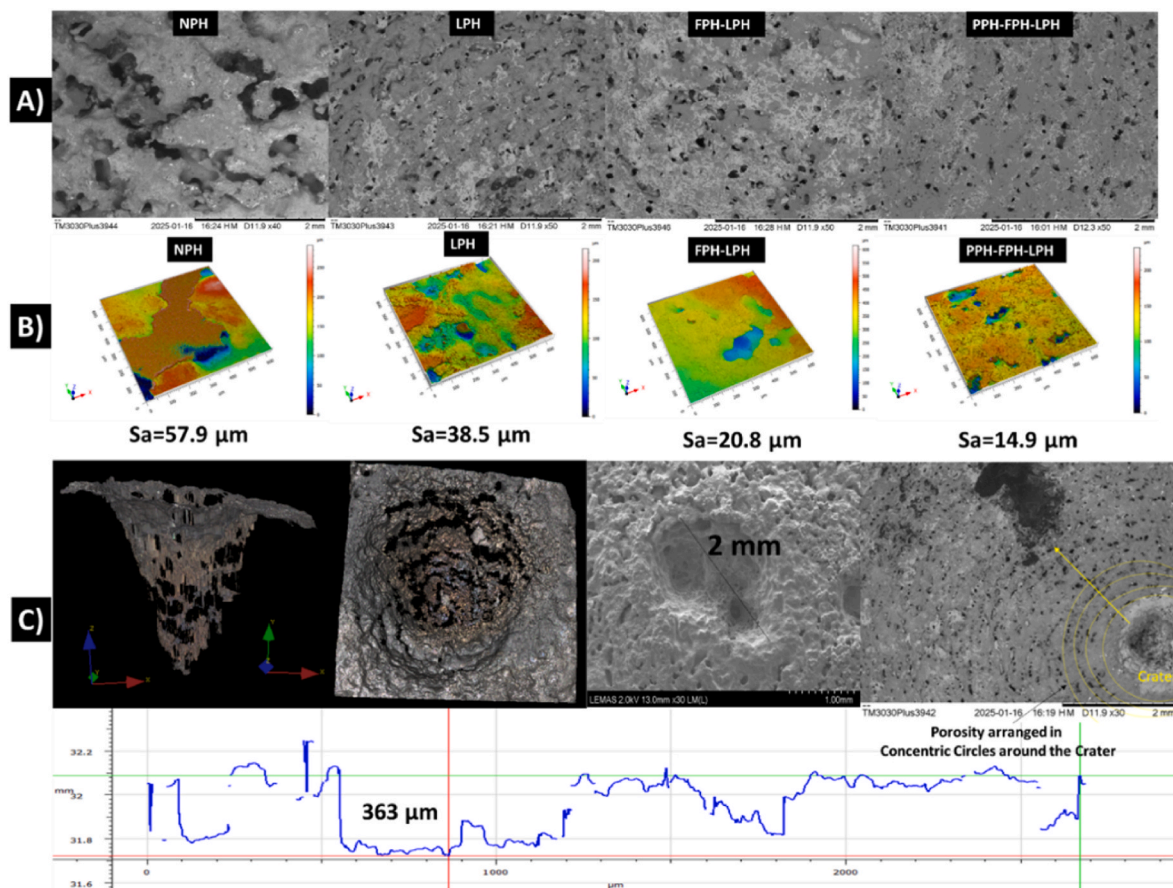


**Fig. 7.** A) The surface morphology of the NPH, LPH, FPH-LPH and PPH-FPH-LPH composites as observed by Scanning Electron Microscopy. B) The surface roughness of the composites as measured using confocal microscopy. C) The ablated crater at the focal point as observed by optical and scanning electron microscopies. Concentric porosity around the crater due to Marangoni convection.

composites reduced progressively with the optimisation of the manufacturing process, with the PPH-FPH-LPH composites demonstrating surface roughness of 14.9  $\mu\text{m}$ . The keyhole crater at the focal point is exhibited in Fig. 7C. The depth of the crater was measured as 363  $\mu\text{m}$ , while the observed porosity was arranged in concentric circles around the crater. The porosity rings were radially distributed, indicating organized melt flow. The porosity pattern corresponded to vapour trapped in the melt, forming bubbles, stemming from the keyhole oscillations [62,63]. The bubbles were advected outward, and were trapped in the solidifying molten pool resulting in voids and porosity, consistent with Marangoni convection driven by surface tension gradients, Fig. 7-C [61,65]. The porosity around the crater was amplified by the rapid degassing and the volume shrinkage during LiChemS [10].

### 3.6. Microstructural analysis

In (Fig. 8 A) the microstructure of an Al reactive particle coated by  $\text{B}_2\text{O}_3$  and  $\text{TiO}_2$  nano-particles is evident. As explained by Daskalakis et al. [10], the milled Al particles reduced the fractured  $\text{TiO}_2$  and  $\text{B}_2\text{O}_3$  nano-particles coating their surface to form  $\text{Al}_2\text{O}_3$  particles coated with  $\text{TiB}_2$  nano-particles. For an adiabatic temperature of 2640 K, all the reactants were present in a liquid form during LiChemS (melting points of  $\text{B}_2\text{O}_3$  – 723 K, Al – 933 K and  $\text{TiO}_2$  – 2103 K), where aluminium reduces the oxides. In (Fig. 8B and C) the microstructure of the  $\text{Al}_2\text{O}_3$ ,  $\text{TiB}_2$  and  $\text{Ti}_2\text{O}_3$  composite was observed in backscattered and secondary electrons modes, while the elemental distribution was confirmed by EDS, Fig. 8 - D. Clusters and fine nano-particles of  $\text{TiB}_2$  with diameter ranging from 10 to 600 nm were dispersed in the  $\text{Al}_2\text{O}_3$  matrix. The dark grey parts corresponded to the  $\text{Al}_2\text{O}_3$  matrix, while the secondary phase

of  $\text{TiB}_2$  was depicted in light grey. The  $\text{Ti}_2\text{O}_3$  phase formed a dendrite type of structure. The particle size of the  $\text{TiO}_2$  and  $\text{B}_2\text{O}_3$  particles defined the particle size of the  $\text{TiB}_2$  phase. The high temperatures developed during LiChemS contributed towards sintering the coated  $\text{Al}_2\text{O}_3$  particles, forming aggregates of  $\text{Al}_2\text{O}_3$  and clusters of  $\text{TiB}_2$  and  $\text{Ti}_2\text{O}_3$ . The dendritic structure of the metastable phase  $\text{Ti}_2\text{O}_3$ , emphasised on the high temperature developed during LiChemS, above the melting point of the  $\text{Ti}_2\text{O}_3$  phase, and the rapid cooling rates characterising the processing method.

Crack networks were observed in the  $\text{Al}_2\text{O}_3$ - $\text{TiB}_2$  matrix with the length ranging between 110 and 160  $\mu\text{m}$ , Fig. 9D and E. In NPH composites cracks blended with the large voids that formed during water and impurities evaporation Fig. 9-A. The cracks were generated in a radial manner matching the thermal propagation of LiChemS. In Fig. 9- B, E the crack propagated through both the  $\text{Al}_2\text{O}_3$  and the  $\text{TiB}_2$ , confirming that both phases acted as a fracture pathway under thermal stress. The keyhole microstructure examined in backscattered electrons mode presented phases heavier than alumina and rich in Ti and Al phases, Fig. 9- C, which were also present at the bottom section of the keyhole, Fig. 9- F.

### 3.7. Mechanical testing

The theoretical Vickers micro-hardness of the composite ( $0.65 \text{ Al}_2\text{O}_3$  –  $0.35 \text{ TiB}_2$ ) was calculated by the rule of mixtures as 1950 HV (19.11 GPa), for Alumina and  $\text{TiB}_2$  Vickers hardness of 10 GPa and 26 GPa respectively [2,3]. The average Vickers micro-Hardness measured by Wilson Hardness equipment was  $1850 \pm 50 \text{ HV}$  ( $18.14 \pm 0.49 \text{ GPa}$ ), according to equation (27), where (F) is the kg-force and (D) is the average of the two diagonals. The Vickers micro-Hardness of the



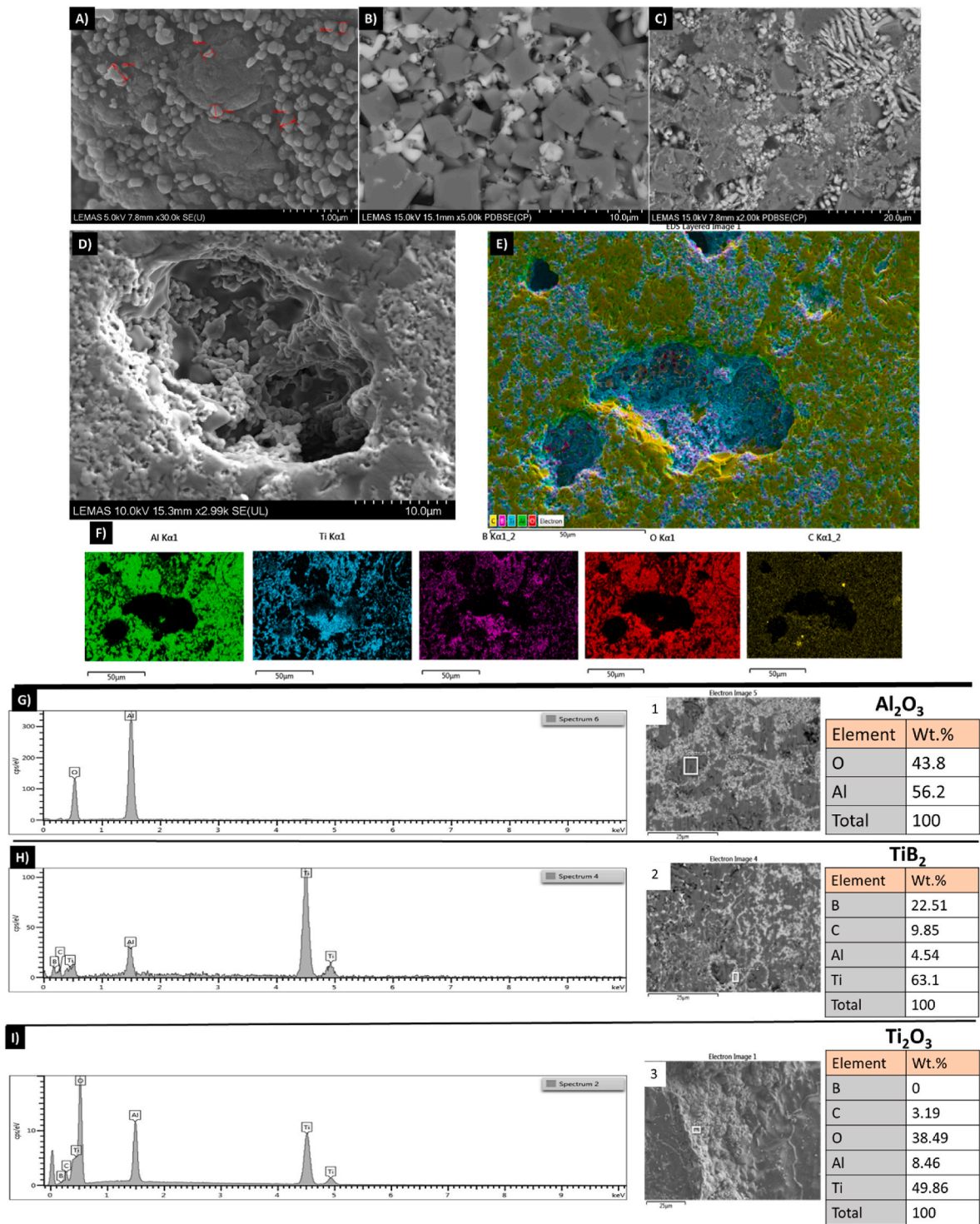


**Fig. 8.** A) The microstructure of an Al particle coated with TiO<sub>2</sub> and B<sub>2</sub>O<sub>3</sub> nanoparticles, in the starting Al-TiO<sub>2</sub>-B<sub>2</sub>O<sub>3</sub> reactant mixture. B), C), D) The TiB<sub>2</sub> and Ti<sub>2</sub>O<sub>3</sub> nano-particles dispersed in the Al<sub>2</sub>O<sub>3</sub> matrix as observed by SEM using backscattered and secondary electron modes. E) and F) The elemental mapping of the Al<sub>2</sub>O<sub>3</sub>-TiB<sub>2</sub> composite. G) Element energy diagram of Al<sub>2</sub>O<sub>3</sub>. H) Element energy diagrams of TiB<sub>2</sub>. I) Element energy diagrams of Ti<sub>2</sub>O<sub>3</sub>.

composites was further confirmed through Scanning Electron Microscopy in secondary electrons mode.

$$HV = 1.854 \left( \frac{F}{D^2} \right) \quad \text{Eq. 27}$$

The length of the diagonals of the indentation spot (300 g) was measured with the assistance of the “Image J”, Fig. 10-A. For an average diagonal length (D) of 17.73 μm, the Vickers micro-hardness was

calculated as 1775 ± 42 HV (17.41 ± 0.41 GPa). The indentation spot did not majorly involve the TiB<sub>2</sub> phase, therefore the Vickers hardness exhibited was lower than the average value identified by the Wilson Hardness equipment. An indentation spot involving the TiB<sub>2</sub> phase, Fig. 10-B, presented a Vickers micro-hardness of 1876 ± 36 HV (18.4 ± 0.35 GPa). EDS analysis verified the presence of the TiB<sub>2</sub> phase, Fig. 10-C. The average Vickers micro-hardness verified by SEM was 1821 ± 45 HV (17.86 ± 0.44 GPa).



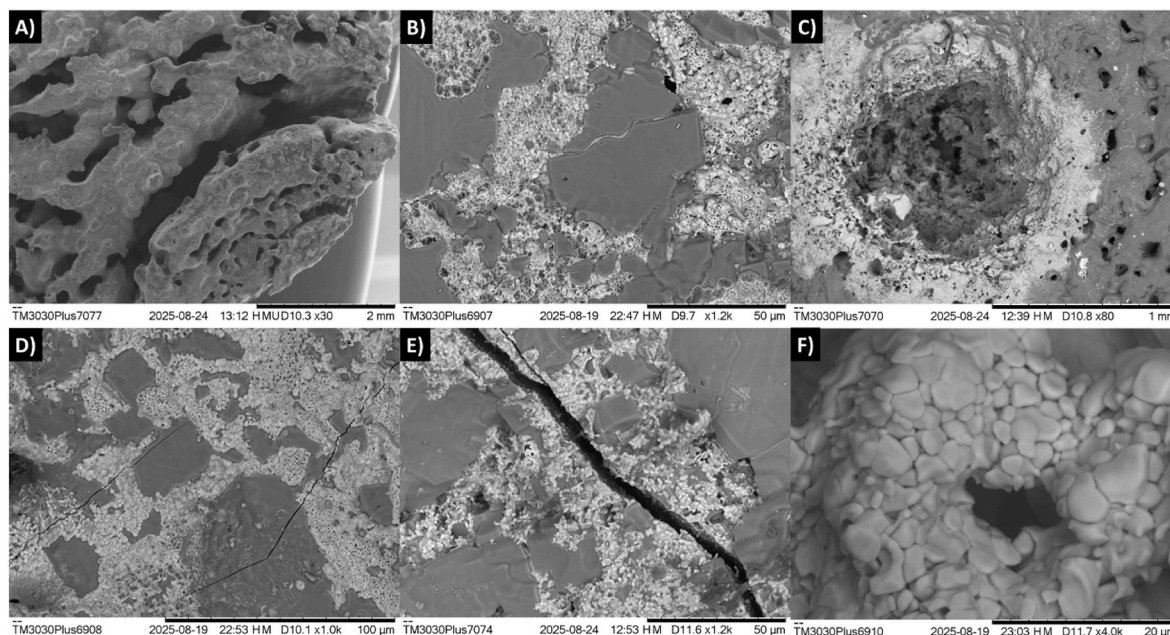


**Fig. 9.** A) Cracks forming on the NPH composites. B) Crack on the Al<sub>2</sub>O<sub>3</sub> grain. C) The keyhole that formed at the focal point. D) Cracks observed on the surface of the Al<sub>2</sub>O<sub>3</sub>-TiB<sub>2</sub> composite of 160 and 110  $\mu$ m length. E) A crack due to thermal stress with a width of 8  $\mu$ m. F) The bottom section of the keyhole.

The fracture toughness of the composite was calculated through equation (28), by measuring the length of the cracks along the diagonals of the indentation produced during Vickers hardness testing. Where (P) is the applied load N, (c) is the crack length starting from the centre of the indentation (m), E is the Young's Modulus (GPa) and (H) is the Vickers Hardness (GPa). For a (c) of 40  $\mu$ m generated by a 2 kg force, the fracture toughness of the composite was calculated as 5.8 MPa·m<sup>1/2</sup>, Fig. 10.

$$K_{IC} = 0.016 \left( \frac{E}{H} \right)^{\frac{1}{2}} \frac{P}{c^{\frac{3}{2}}} \quad \text{Eq.28}$$

The compressive strength of the NPH, LPH, FPH-LPH and PPH-FPH-LPH composites (N = 12), was compared to Al<sub>2</sub>O<sub>3</sub> compacts (250 MPa) sintered at 1573 K for 8 h.

The Stress/Strain plots of the optimum NPH, LPH, FPH-LPH and PPH-FPH-LPH composites are displayed in Fig. 10. The NPH composites demonstrated multiple matrix fractures across the whole range of strain induced to the composite, due to their expanded structure and low density, before failing at 93 MPa. The LPH and FPH-LPH composites presented minor matrix fractures at low strain, mostly attributed to minor inconsistencies with the flatness of the composites, before failing at 211 and 230 MPa respectively. The FPH-LPH composites with pre-existing cracks failed at lower stress of 155 MPa. The optimum PPH-FPH-LPH composites exhibited greater compressive strength than sintered alumina pellets, fracturing at 350 MPa compared to 306 MPa. The matrix fractures and failures observed during the compressive tests were not sharp, indicating good interfacial bonding between the Al<sub>2</sub>O<sub>3</sub>-TiB<sub>2</sub> phases [37,38]. The addition of TiB<sub>2</sub> to the alumina matrix improved the fracture toughness of the composite.

The impact resistance performance of the optimum PPH-FPH-LPH composites (N = 5) was evaluated using drop ball impact testing. The maximum theoretical height required to prevent the fracture of the Al<sub>2</sub>O<sub>3</sub>-TiB<sub>2</sub> composite disks (D = 20 mm, Thickness = 4 mm) was correlated to the defect sizes within the composites, Fig. 10-J, using the analytical model in Materials and Methods 2.3 and Supplementary S2.2, that employs Hertzian Contact Mechanics and the Contact Mechanics [42,46]. The results from the ball drop impact testing, including the energy absorbed by the composite and the velocity of the stainless

steel balls at impact, are summarised in Table 4. The composites withstood 89.2, 148.9 and 174 N before fracturing from the respective heights of 0.65 m (14 g), 0.2 m (66 g) and 0.08 m (178 g). The composites fractured into multiple pieces (3 to 8 large pieces) at impact, which is desired for energy absorption during impact resistance experiments.

The craters and cracks generated at the impact site were observed through SEM, Fig. 11 A. Fig. 11 B, C demonstrates cracks generated at the contact radius (D = 600  $\mu$ m), inflicted by the 14 g stainless steel ball. In Fig. 11D and E, crack propagation was observed at a radius of approximately 0.85 mm from the impact point. The cross section of a fractured piece is observed at Fig. 11 F.

A summary of the processing-properties relationship of the optimum i) NPH, ii) LPH, iii) FPH-LPH and iv) PPH-FPH-LPH composites is displayed in Fig. 12.

## 4. Discussion

### 4.1. LIChemS mechanism

The research conducted herein, demonstrates the potential of LIChemS in manufacturing high purity and density Al<sub>2</sub>O<sub>3</sub>-TiB<sub>2</sub> composites, through a processing methodology that can also be implemented for synthesising composites such as Al<sub>2</sub>O<sub>3</sub>-B<sub>4</sub>C/WC/ZrB<sub>2</sub>. Conventional methods in the literature for manufacturing the Al<sub>2</sub>O<sub>3</sub>-TiB<sub>2</sub> composite involve energy-demanding solid, liquid, and vapour state in-situ [5–14, 16,17,19–22,24,26] and ex-situ [15,18,23,25,28] processes. Laser ignition synthesis has been previously employed for synthesising alloys rather than hard ceramic materials, where high laser powers were utilised for generating sufficient plasma for combustion [55–59,74–77].

LIChemS mechanism in the Al-TiO<sub>2</sub>-B<sub>2</sub>O<sub>3</sub> system, Fig. 13, initiated with the heterogeneous photon absorption by the conduction electrons of aluminium (Drude mechanism) [80], which oscillated in response to the electromagnetic radiation of the CW laser that penetrated within a few nm depth [80]. The oscillating phenomenon was progressively amplified by the microstructure of the Al micro-particles, coated with fractured TiO<sub>2</sub> and B<sub>2</sub>O<sub>3</sub> nanoparticles ( $\leq 600$  nm), as the defects and surface roughness introduced through milling enhanced light trapping.

The hygroscopic B<sub>2</sub>O<sub>3</sub> further increased the absorbance of the

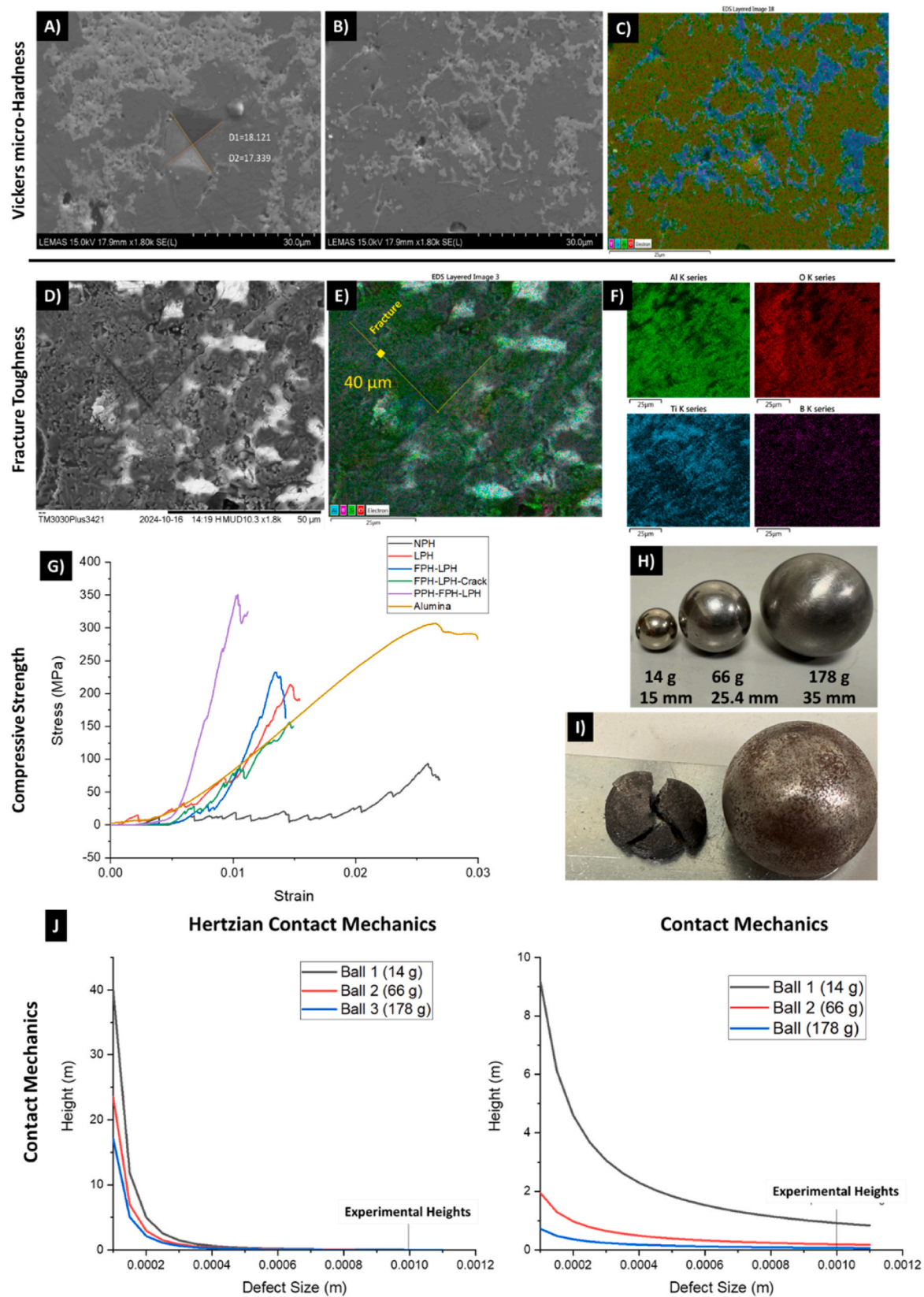


**Fig. 10.** A) Indentation on an alumina-rich spot. B) Indentation on a spot displaying well dispersed  $\text{TiB}_2$  phase in the  $\text{Al}_2\text{O}_3$  matrix. C) EDS analysis of the indentation spot. D) Indentation demonstrating crack propagation at the diagonals for fracture toughness analysis. E) and F) EDS analysis of the indentation point. G) Compressive strength comparison of the NPH, LPH, FPH-LPH and PPH-FPH-LPH composites with pure alumina composites (250 MPa) sintered at 1573 K for 10 h. H) The stainless steel balls used during drop ball impact testing. I) Fractured  $\text{Al}_2\text{O}_3$ - $\text{TiB}_2$  composite by the 178 g stainless steel ball. J) The experimental drop heights for the three stainless steel balls in correlation to the defect size in the composites.



Table 4

The experimental drop heights, impact energy and velocity of the stainless steel balls at impact during the ball drop impact testing.

| Ball Mass (g) | Experimental Height 2 (m) | Number of Samples Fractured | Energy at Impact (J) | Force at Impact (N) | Velocity at Impact (m/s) |
|---------------|---------------------------|-----------------------------|----------------------|---------------------|--------------------------|
| 14            | 0.65                      | 1 of 5                      | 0.089                | 89.2                | 3.62                     |
| 66            | 0.2                       | 3 of 5                      | 0.148                | 148.9               | 2.12                     |
| 178           | 0.08                      | 4 of 5                      | 0.174                | 174                 | 1.4                      |

Table 5

Laser intensities used in the literature for triggering self-sustaining reactions.

| No | Reference         | Laser Power (W) | Area Beam Spot (mm <sup>2</sup> ) | Intensity (W/mm <sup>2</sup> ) |
|----|-------------------|-----------------|-----------------------------------|--------------------------------|
| 1  | Biffi et al. [55] | 200 W           | -                                 | -                              |
| 2  | Li et al. [56]    | 1600 W          | 352 mm <sup>2</sup>               | 4.54                           |
| 2  | Li et al. [57]    | 1200 W          | 100 mm <sup>2</sup>               | 12                             |
| 3  | Li et al. [75]    | -               | -                                 | -                              |
| 3  | Feng et al. [76]  | 100 W           | 0.031 mm <sup>2</sup>             | 3225                           |
| 4  | Li et al. [58]    | 100 W           | 0.031 mm <sup>2</sup>             | 3225                           |
| 4  | Qin et al. [77]   | 1600 W          | 352 mm <sup>2</sup>               | 4.54                           |
| 5  | Hunt et al. [59]  | 50 W            | -                                 | -                              |
| 6  | An et al. [60]    | 1000 W          | 78 mm <sup>2</sup>                | 12.73                          |
| 7  | This Research     | 15 W            | 15.9 mm <sup>2</sup>              | 0.94                           |

mixture through the humidity intrinsically present in the H<sub>3</sub>BO<sub>3</sub> phase [10]. With the H<sub>3</sub>BO<sub>3</sub> decomposition at 170 °C porosity and voids formed on the surface of B<sub>2</sub>O<sub>3</sub> [81], further enhancing light absorption. The transient dehydration of the mixture promoted early-stage electro-phonon thermal coupling, before the subsequent melting of B<sub>2</sub>O<sub>3</sub> (450 °C) and Al (660 °C).

The molten pools of B<sub>2</sub>O<sub>3</sub> and Al enhanced the absorbance of the reactants and increased internal reflections, with the liquid phase acting as a primitive keyhole cavity [61,62], setting the conditions for ignition.

Within the keyhole cavity, multiphoton-assisted absorption in the heated oxides took place [61–63] and once the reaction threshold was exceeded, the thermite reaction self-propagated, releasing sufficient energy to mimic welding-like conditions [1,29], despite the modest laser intensity of 1.13 W/mm<sup>2</sup> used during LIChemS. The formation of narrow-bandgap intermediate products such as Ti<sub>2</sub>O<sub>3</sub> (phase transformation), further promoted the conversion of light to heat. The vigorous evaporation of phases during LIChemS generated recoil pressure which deepened the keyhole and trapped the incident laser beam [61–63].

The confined Al/Ti vapours continuously absorbed energy from the multiple internal reflections of the incident beam [61,64] and the exothermicity of the reaction [1,29], increasing the local energy density at the focal point, leading to the formation of a luminous, partially

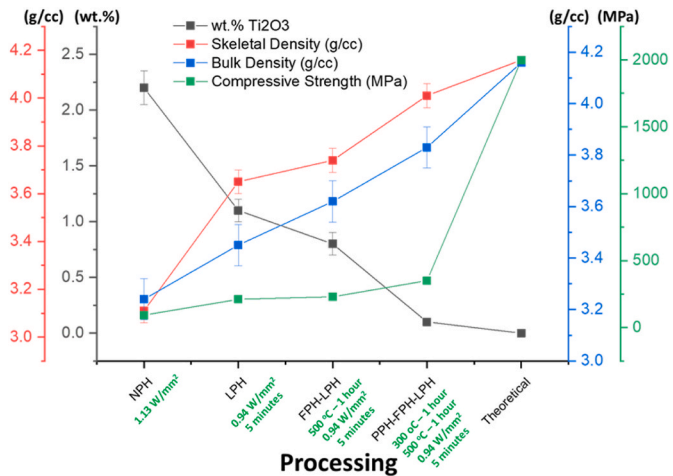


Fig. 12. The processing-properties relationship of the NPH, LPH, FPH-LPH, PPH-FPH-LPH composites in relation to i) Ti<sub>2</sub>O<sub>3</sub> wt.%, ii) skeletal and iii) bulk densities and iv) compressive strength.

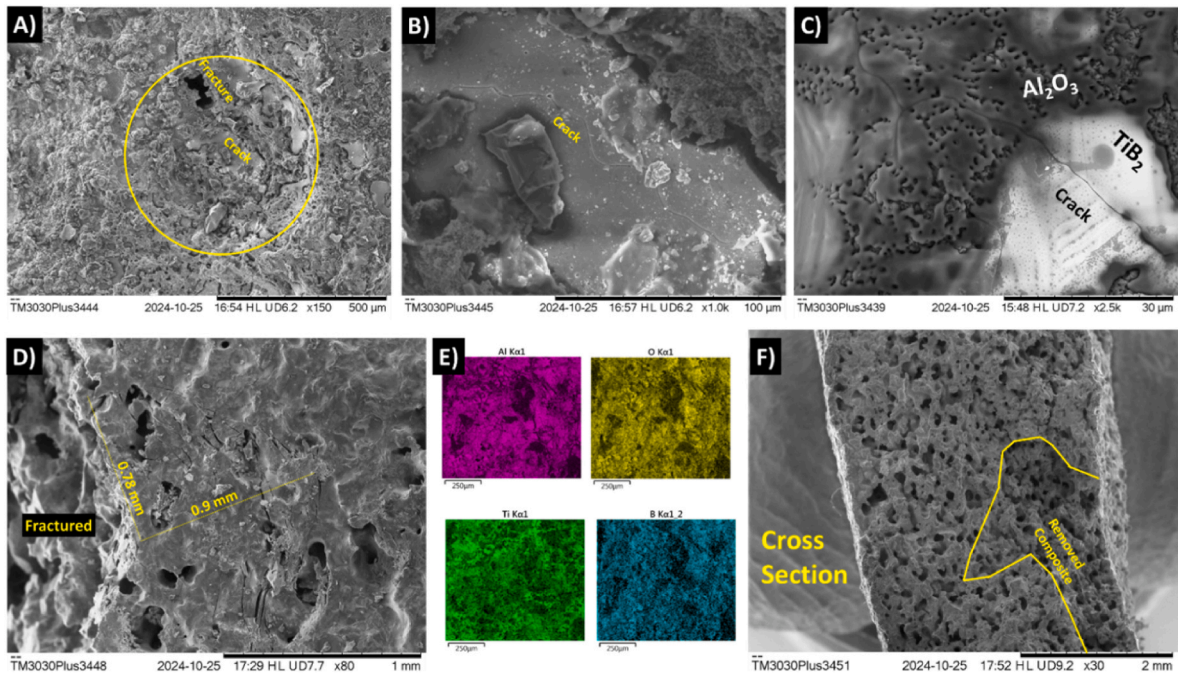
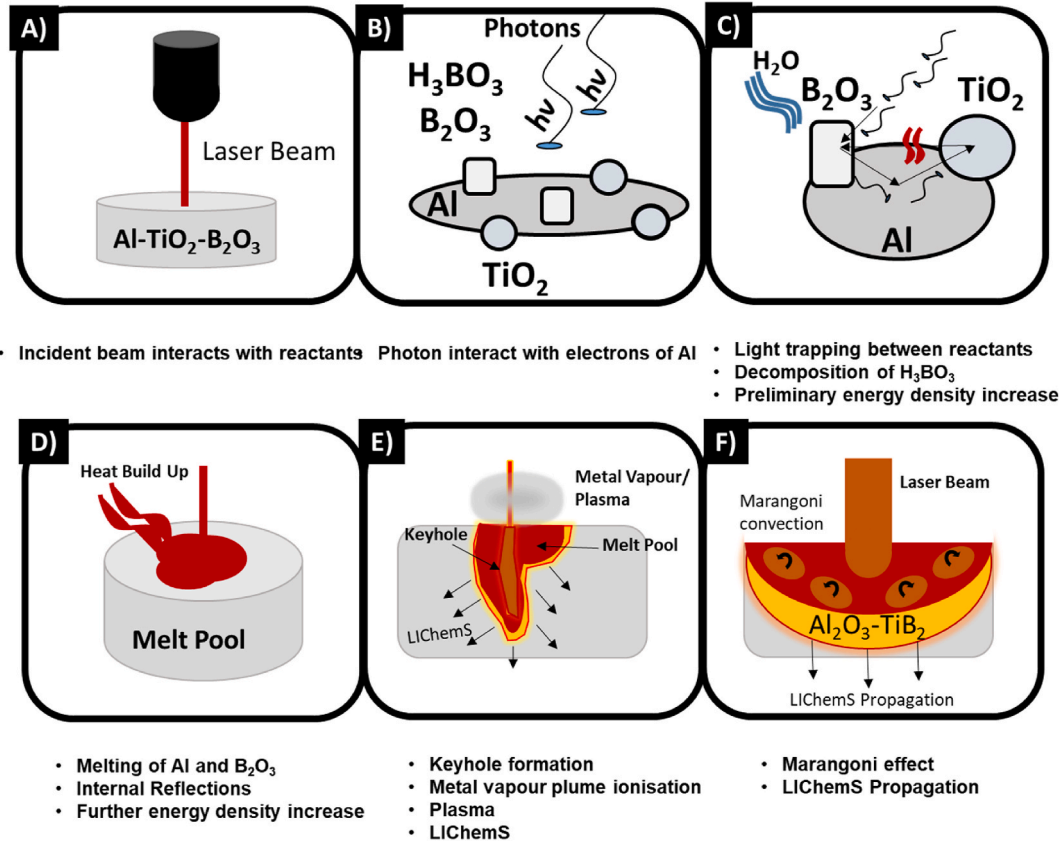


Fig. 11. A) Crater forming due to the impact of the stainless steel ball with the surface of the Al<sub>2</sub>O<sub>3</sub>-TiB<sub>2</sub> composite. B) and C) Micro-cracks present in the impact crater. D) The radius of impact in the Al<sub>2</sub>O<sub>3</sub>-TiB<sub>2</sub> composite (0.85 μm) for the 178 g ball. E) EDS mapping for elemental distribution at the fracture point. F) Cross section of a fractured piece.

## LiChemS Mechanism



**Fig. 13.** The mechanism of LiChemS. A) Sample-laser beam interaction. B) Photon interaction with conducting electrons of Al. C) Light scattering between reactants. D) Material heating and melt pool formation. E) Keyhole formation and metal vapour thermal ionisation for plasma generation. LiChemS onset. F) Marangoni convection and LiChemS propagation.

ionised metal vapour plume of several thousand kelvin (i.e plasma).

Then Marangoni convection [61,64], driven by strong temperature gradients in surface tension, organised the melt flow into toroidal rolls aligned with radial isotherms. Periodic oscillations of the keyhole compressed vapour bubbles, which were advected outward and trapped in the solidifying melt, yielding concentric porosity rings around the ablation crater as the exothermic front decayed radially. Therefore, the plasma generation and porosity zoning present in the ablated crater did not derive from direct multiphoton absorption but from the interplay of i) the melt pool formation, ii) vapour plumes confinement in the keyhole, iii) light scattering and reaction exothermicity, and iv) vapour ionisation. The plasma generated at the irradiation point [53] propagated energy via electrons/ions –phonon coupling, lattice vibrations, convective flow and radiation. The prevalence and lifetime of the generated plasma depended on i) maintaining local power density above the reaction threshold and ii) on the available reactant volume [54].

For a sample of 10 mm in diameter and 3 mm thickness, the heat wave required 2 s to propagate across the compact, while the thermal decay from the adiabatic temperature to 473 K lasted approximately 9–12 s. Table 5 demonstrated the significant difference in the magnitude of the laser intensity used in this research and the literature, sometimes reaching 10<sup>3</sup> (W/mm<sup>2</sup>) grade of magnitude [55–60,74–77].

The selection of the reactive mixture (Al-TiO<sub>2</sub>-B<sub>2</sub>O<sub>3</sub>) was based on its potential to provide sufficient exothermicity for sustaining the propagation of the reaction across the volume of the sample. The enthalpy of reaction for the reaction mechanisms of the literature (Supplementary S1.1) was calculated by equation (29) and is summarised in Table 6.

$$\Delta H_{\text{reaction}} = \sum \Delta H_f^{\circ}(\text{Products}) - \sum \Delta H_f^{\circ}(\text{Reactants}) \quad \text{Eq.29}$$

**Table 6**

The enthalpy of exothermic reactions for producing the Al<sub>2</sub>O<sub>3</sub>-TiB<sub>2</sub> composite.

| Literature                                          | Reaction                                                                                                                                                                                              | $\Delta H$ (298 K)<br>(kJ/mol) |
|-----------------------------------------------------|-------------------------------------------------------------------------------------------------------------------------------------------------------------------------------------------------------|--------------------------------|
| Mohammad Sharifi et al. [5]<br>Sundaram et al. [34] | $10 \text{ Al} + 3 \text{ TiO}_2 + 3 \text{ B}_2\text{O}_3 = 5 \text{ Al}_2\text{O}_3 + 3 \text{ TiB}_2$                                                                                              | –2728                          |
| Sharifi et al. [6]                                  | $2 \text{ Al} + \text{B}_2\text{O}_3 + \text{Ti} = \text{Al}_2\text{O}_3$ (56 wt.%) + $\text{TiB}_2$ (44%)                                                                                            | –729                           |
| Khaghani et al.                                     | $\text{TiO}_2 + 2 \text{ H}_3\text{BO}_3 + \frac{10}{3} \text{ Al} = \frac{5}{3} \text{ Al}_2\text{O}_3 + \text{TiB}_2 + 3 \text{ H}_2\text{O}$                                                       | –715                           |
| This Research                                       | $\frac{22}{3} \text{ Al} + 4 \text{ TiO}_2 + \text{B}_2\text{O}_3 + 2 \text{ H}_3\text{BO}_3 = \frac{11}{3} \text{ Al}_2\text{O}_3 + 2 \text{ TiB}_2 + \text{Ti}_2\text{O}_3 + 3 \text{ H}_2\text{O}$ | –1864                          |

The adiabatic temperature of the reaction was calculated as 2643 K, and it is in accordance with the ones reported in the literature, Table 7 [5,6,11,13,17,20].

### 4.2. Phase analysis and reaction mechanism

Previously conducted research suggests a variety of reaction mechanisms for manufacturing the Al<sub>2</sub>O<sub>3</sub>-TiB<sub>2</sub> composite Supplementary S1.1, and they all agree on the aluminum-mediated reduction of B<sub>2</sub>O<sub>3</sub> and TiO<sub>2</sub>, for the formation of TiB<sub>2</sub> inside the alumina matrix [5–7,22,33,34]. “Slow” in situ processing techniques have produced low purity Al<sub>2</sub>O<sub>3</sub>-TiB<sub>2</sub> composites containing aluminoborate phases such as

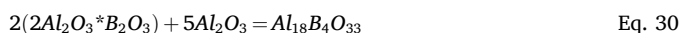


**Table 7**

Comparison of the adiabatic temperature calculated in this research with those in the literature.

| Literature                  | Composition                                                                                   | Adiabatic Temperatures (K) |
|-----------------------------|-----------------------------------------------------------------------------------------------|----------------------------|
| Mohammad Sharifi et al. [5] | Al <sub>2</sub> O <sub>3</sub> - 29 wt% TiB <sub>2</sub>                                      | 2812                       |
| Sharifi et al. [6]          | Al <sub>2</sub> O <sub>3</sub> - 44 wt% TiB <sub>2</sub>                                      | 2783                       |
| Mousavian et al. [11]       | Al <sub>2</sub> O <sub>3</sub> - 29 wt% TiB <sub>2</sub>                                      | 2573                       |
| Wang [13]                   | (Al <sub>2</sub> O <sub>3</sub> /TiB <sub>2</sub> ) - 30 wt% SiO <sub>2</sub>                 | 2314                       |
| Meyers et al. [17]          | Al <sub>2</sub> O <sub>3</sub> - 29 wt% TiB <sub>2</sub>                                      | 2448                       |
| Yu. Popov et al. [20]       | Al <sub>2</sub> O <sub>3</sub> - 29 vol% TiB <sub>2</sub>                                     | 4073                       |
|                             | Al <sub>2</sub> O <sub>3</sub> - 35 vol.% B <sub>4</sub> C                                    |                            |
| This Research               | Al <sub>2</sub> O <sub>3</sub> - TiB <sub>2</sub> (traces of Ti <sub>2</sub> O <sub>3</sub> ) | 2643                       |

Al<sub>18</sub>B<sub>4</sub>O<sub>33</sub> and Al<sub>5</sub>BO<sub>9</sub>. Ray et al. observed the formation of the Al<sub>5</sub>BO<sub>9</sub> phase starting at 1073 K, while at 1373 K, the Al<sub>18</sub>B<sub>4</sub>O<sub>33</sub> phase began forming at the expense of Al<sub>5</sub>BO<sub>9</sub> [82] according to equation (30).

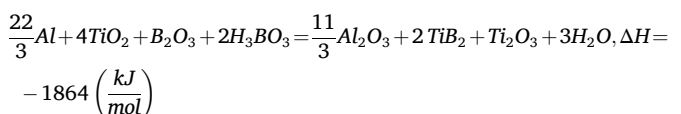


The findings align with those of Daskalakis et al. [10]. Furnace-synthesised composites (1673 K) derived from the same reactive mixture (Al-TiO<sub>2</sub>-H<sub>3</sub>BO<sub>3</sub>/B<sub>2</sub>O<sub>3</sub>) used in this research exhibited both the Al<sub>18</sub>B<sub>4</sub>O<sub>33</sub> and Al<sub>5</sub>BO<sub>9</sub> phases. Further heat treatment of the composites for 1 h at 1473 K increased the Al<sub>18</sub>B<sub>4</sub>O<sub>33</sub> phase to ~20 wt%. In contrast the rapid heating and cooling rates of LiChemS presented herein, limited the formation of intermediate aluminaborate compounds such as Al<sub>18</sub>B<sub>4</sub>O<sub>33</sub> and Al<sub>5</sub>BO<sub>9</sub> [10].

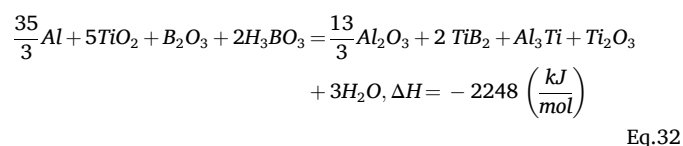
Daskalakis et al. [10] identified that B<sub>2</sub>O<sub>3</sub> absorbed atmospheric water to form H<sub>3</sub>BO<sub>3</sub>, and therefore the starting mixture was described as Al-TiO<sub>2</sub>- (B<sub>2</sub>O<sub>3</sub> - 24 wt% H<sub>3</sub>BO<sub>3</sub>), which compromised the stoichiometric mass of boron. During NPH-LiChemS, the violent degassing of water, B<sub>2</sub>O<sub>3</sub> and H<sub>3</sub>BO<sub>3</sub> further depleted stoichiometric boron and led to the formation of Ti-O and Al-Ti by-products [33,34], such as the metastable phase of Ti<sub>2</sub>O<sub>3</sub>, and Al<sub>3</sub>Ti. NPH performed at high laser intensities intensified the degassing phenomenon.

The synthesis of the Ti<sub>2</sub>O<sub>3</sub> metastable phase was associated with the rapid heating and cooling rates of the self-propagating high-temperature synthesis (SHS). The aluminothermic reduction of TiO<sub>2</sub> typically proceeds through intermediate oxides of Ti<sub>3</sub>O<sub>5</sub> (1273–1473 K), Ti<sub>2</sub>O<sub>3</sub> (1473–1773 K) and TiO (>1773 K) [83,84]. The Ti<sub>2</sub>O<sub>3</sub> is less thermodynamically stable than TiO<sub>2</sub> and TiO, but its formation can be favoured under rapid heating and cooling, as it can nucleate faster than the thermodynamically stable phases [83,84]. Rapid cooling prevents all of the titanium from been reduced to form TiB<sub>2</sub>, leaving the Ti<sub>2</sub>O<sub>3</sub> metastable phase in the matrix [85].

We employed convective heating and laser processing for dissolving the H<sub>3</sub>BO<sub>3</sub> phase, calcinate and sinter the reactants prior to LiChemS. LPH efficiently produced high purity composites in a laboratory setting (traces of Ti<sub>2</sub>O<sub>3</sub>, D = 5–20 cm, m = 0.5–5 g). However it might not be as successful in a scaled-up process, as the highest permissible laser intensity for performing LPH is influenced by 2 factors: i) Not surpassing the ignition threshold, and ii) removing boron oxide at the focal point. Convective heating was efficient in drying compacts of larger mass, while drying the reactants prior to compaction produced the highest purity Al<sub>2</sub>O<sub>3</sub>-TiB<sub>2</sub> composites. Compositional analysis of LiChemS-composites [10,86], suggest minor scale side reactions taking place, equation (31). The yields of Al<sub>2</sub>O<sub>3</sub>, TiB<sub>2</sub> and Ti<sub>2</sub>O<sub>3</sub>, and the exothermicity of the reactions are calculated in the Supplementary S4.1.



For non-optimised laser parameters and increased (wt.%) of H<sub>3</sub>BO<sub>3</sub> in the starting mixture, the reaction mechanism is described by equation (32).



### 4.3. Density and structure comparison

Across the literature, densification processes provided Al<sub>2</sub>O<sub>3</sub>-TiB<sub>2</sub> composites with the highest relative density 90–99 % [16,17,19,20]. LiChemS composites lay within this margin of 96 % skeletal density and 92 % bulk density. In-situ manufacturing processes nevertheless are bound to produce composites displaying higher porosity compared to ex-situ processes. This was attributed to i) dislocations forming in the matrix, ii) grains intrinsic porosity, iii) porosity in the grain boundaries, iv) volume reduction (–28 % in the case of the Al<sub>2</sub>O<sub>3</sub>-TiB<sub>2</sub> composite) and v) thermal stresses accompanying SHS [69,78]. Degassing also contributed into forming intra-granular voids [16,17,19]. In this research two additional factors contributed towards the final porosity: i) the structural defects induced during cold pressing and ii) Marangoni convection.

Since laser ignition synthesis is a pressureless manufacturing process, the compaction parameters during cold pressing directly affected the density of the composites (See Supplementary S2.1). In the literature, the relative green density of the reactants was reported as 50 % [14], 60 % [11] and 70 % [17], for the application of 100, 400 and 110 MPa pressures respectively. In this research, a range of pressures between 74 and 1000 MPa were applied during cold pressing, with 250 MPa (relative density of ~70 %) providing the optimum density composite. Pressures below 250 MPa compromised on the density, while pressures greater than 250 MPa compromised the green density of the reactants, generating defects and introducing porosity.

NPH generated voids, while LPH and FPH generated macro-cracks, evident by the CT scans, Fig. 6. Similarly during hot-pressing, Kecskes et al. [16], confirmed the presence of large voids at the centre of the sample, due to outgassing of water, H<sub>3</sub>BO<sub>3</sub> and B<sub>2</sub>O<sub>3</sub>. Still FPH prior to LiChemS enhanced the overall density of the Al<sub>2</sub>O<sub>3</sub>-TiB<sub>2</sub> composite (4.01 g/cc PPH - FPH-LPH) compared to (3.84 g/cc PPH-LPH), at the cost of increasing the processing time and energy consumption of the manufacturing process.

Chen et al. investigated the origin of crack evolution in ceramics during cooling [87], concluding that slow cooling produced a larger temperature gradient between the surface and the centre, leading to progressive fracture initiation at weak points, forming a dense, intersecting microcrack network, which was in accordance with findings previously reported during furnace [88] and hot pressing processing [17]. In the contrary, rapid cooling, also observed during LiChemS, resulted in rapid crack propagation forming fewer but larger fractures [87], Fig. 9.

Employing a Newtonian cooling model we identified that a differential temperature of 349 K between the centre and the edges was sufficient to exceed the fracture strength of the composite. The thermal mismatch was evident in the cracks observed in Fig. 9. Cracks propagated through both phases, under rapid cooling, consistent with the stress-driven fracture process across phases with different stiffness and expansion coefficients [89]. The NPH composites mostly presented a crack network mostly resembling interconnected porosity, due to the significant material removal during LiChemS. The cracks were arranged in a radial configuration following the thermal decay of the LiChemS wave, contrary to the PPH-LPH-FPH samples that the crack generation did not follow an organised pattern.

#### 4.4. Microstructural characterisation and surface profile

The coating of  $\text{TiO}_2$  and  $\text{B}_2\text{O}_3$  nano-particles was reduced by the aluminium micro particle substrates to form  $\text{Al}_2\text{O}_3$  particles coated by  $\text{TiB}_2$  nano-particles. The heat generated by LIChemS sintered the coated  $\text{Al}_2\text{O}_3$  particles, forming structures consisting of aggregates of  $\text{Al}_2\text{O}_3$  and  $\text{TiB}_2$ . The particle size of  $\text{TiO}_2$  defined the size of the  $\text{TiB}_2$  particles which agrees with the literature [16,21]. Contrary to in-situ hot-pressed  $\text{Al}_2\text{O}_3$ - $\text{TiB}_2$  composites, featuring  $\text{TiB}_2$  aggregates at the central regions of the composites and fine  $\text{TiB}_2$  particles at the edges, the microstructure of the LIChemS  $\text{Al}_2\text{O}_3$ - $\text{TiB}_2$  composites relied on the size of the coated aluminium micro particles. Ideally submicron Al particles coated with nano-particles of  $\text{TiO}_2$  and  $\text{B}_2\text{O}_3$  could provide a microstructure displaying well dispersed, fine  $\text{TiB}_2$  nano-particles in the  $\text{Al}_2\text{O}_3$  matrix. The surface roughness of the LIChemS composites (14  $\mu\text{m}$ ) was improved with employing effective methods of dissolving  $\text{H}_3\text{BO}_3$  prior to LIChemS.

The keyhole at the focal point had a depth of 363  $\mu\text{m}$  and exhibited concentric porosity rings, observed via SEM. The rings were attributed to the keyhole dynamics, where recoil pressure from intense evaporation formed a cavity that oscillated [61,62]. Marangoni convection trapped vapours into toroidal flows, which aligned with radial isotherms, during solidification [53]. The Gaussian beam profile enhanced localized heating at the focal point [90], initiating the keyhole and amplifying thermite-driven energy release which sustained these patterns.

#### 4.5. Mechanical properties comparison

The Vickers micro-Hardness and fracture toughness of the LIChemS composites were measured as 1850 HV ( $18.14 \pm 0.49$  GPa- 95 %) and  $5.8 \text{ MPa m}^{-2}$ , among the highest in the literature [10,11,15–20]. They were superior to the ones by conventional sintering and within the range of composites produced by densification processes. The effective strength of porous  $\text{Al}_2\text{O}_3$  (48 %) and (27 %) was reported as 17.63 to 137 MPa [37] by Suleiman et al. Shuai et al. [38] identified a compressive strength of 142 MPa of alumina lattice structures synthesised through digital light processing. The compressive strength of ( $\text{TiB}_2$ ) was measured as 1.1 GPa and 1.8 GPa for densities of 3.8 g/cc and 4.51 g/cc respectively, by Murno [36]. The optimum compressive strength of the PPH-FPH-LPH ( $\text{Al}_2\text{O}_3$ -29 wt% $\text{TiB}_2$ ) composites in this research was reported as 350 MPa, 15 % greater than the compressive strength of monolithic alumina sintered at 1200 °C for 10 h.

In the literature, the impact resistance performance of the  $\text{Al}_2\text{O}_3$ - $\text{TiB}_2$  composites was correlated the effective strength (static and dynamic compressive strengths divided by the density) [42], fracture toughness [43] and density [44,45] of the composites. The generation of fractures was attributed to i) trans-granular and intergranular fracture of the  $\text{Al}_2\text{O}_3$  matrix and ii) poor interfacial bonding [43,45]. The

PPH-FPH-LPH composites synthesised in this research, with density of 4.16 g/cc, fracture toughness of  $5.8 \text{ MPa m}^{-2}$  and compressive strength of 350 MPa withstood 174 N before fracturing. The critical energy release rate (Gc), was calculated according to equation (33), indicating that 8 mJ are required for generating 1  $\text{cm}^2$  of crack [91].



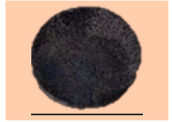

$$\left(G_c = \frac{K_{IC}^2}{E}\right) = 80 \text{ J} / \text{m}^2 \quad \text{Eq. 33}$$

#### 4.6. Energy consumption and scale up challenges

The energy efficiency of each (LIChemS) process employed in this research (PPH-NPH, PPH-LPH, PPH-FPH-LPH), was compared to the one of conventional sintering, provided by Daskalakis et al. [10], in Table 8. The energy consumption calculations were conducted on the basis that the reactants were milled and dried for all processes. NPH composites were manufactured for laser powers greater than 18 W for 1 s of exposure, indicating that 18 J were sufficient for their synthesis. The silica tube furnace was purged with argon for 2 min at 1L/min flowrate before the ignition takes place and the composite was kept at inert conditions for 2 min after ignition, therefore a total of 4 L of argon gas was required. The optimum LPH composites were synthesised within 9 min which involved: i) purging the silica tube with argon, ii) laser processing the reactants, iii) LIChemS and iv) cooling. The process required 3–4.5 kJ for its completion and 9 L of argon gas. When furnace sintering was also incorporated in the process, performed by a conventional carbolite furnace (~4 kWh), then the energy consumption of the process increased to  $1.44 \times 10^3$  kJ. The duration of the process was prolonged to 1 h and 9 min, while the argon consumption remained at 9 L. Conventional furnace sintering as reported by Daskalakis et al. [10] required 3 h and 40 min, energy equal to  $5.28 \times 10^3$  kJ and 880 L of argon gas. The comparison of the energy and gas consumption of each process, along with the specifications of each sample are summarised in Table 8.

In this research, the scalability potential of the LIChemS technology has been demonstrated in a laboratory setting (20 mm pellet –3 g), however integrating the technology in an industrial scale process entails challenges. The main challenge is the thermal runaway, stemming from the rapid heat generation ( $10^4$  to  $10^5$  K/s) in comparison to the heat loss, which can lead to equipment overheating [1,29]. The high temperatures developed (2000–5000K) [30] during processing can alter the stoichiometry degrading the purity of the product. When processing greater volumes of material, the non-uniform temperature distribution, could lead to greater differential temperatures between the core and edges inducing cracks [69], compromising the density and microstructure of the products. Gas evolution during LIChemS can also get intensified generating porosity, residual stresses and weak interfacial bonding between phases [69]. Mitigation strategies primarily involve removing the

**Table 8**  
The duration, energy and gas consumption of each manufacturing process, along with the composition, density and Vickers micro-hardness of the produced composites.

| Manufactured Composites      |  |  |  |  |
|------------------------------|-------------------------------------------------------------------------------------|-------------------------------------------------------------------------------------|---------------------------------------------------------------------------------------|---------------------------------------------------------------------------------------|
| Technique                    | PPH-NPH                                                                             | PPH-LPH                                                                             | PPH-FPH-LPH                                                                           | Conventional Furnace [10]                                                             |
| By Product Phases            | 1.8 wt% $\text{Ti}_2\text{O}_3$                                                     | 0.6 wt% $\text{Ti}_2\text{O}_3$                                                     | 0.1 wt% $\text{Ti}_2\text{O}_3$                                                       | (<20 wt%) $\text{Al}_5\text{BO}_9$ , $\text{TiBO}_3$                                  |
| Density (g/cc)               | 3.48                                                                                | 3.84                                                                                | 4.01                                                                                  | 2.98                                                                                  |
| Vickers micro-Hardness (GPa) |                                                                                     | $18.14 \pm 0.49$                                                                    |                                                                                       | $12.95 \pm 0.39$                                                                      |
| Laser Processing Time (s)    | 1                                                                                   | 300                                                                                 | 300                                                                                   | -                                                                                     |
| Laser Power (W)              | 18–30                                                                               | 10–15                                                                               | 10–15                                                                                 | -                                                                                     |
| Furnace Processing Time (s)  | -                                                                                   | -                                                                                   | 3600                                                                                  | 13200                                                                                 |
| Furnace Power (Wh)           | -                                                                                   | -                                                                                   | 4000                                                                                  | 4000                                                                                  |
| Energy (J)                   | 18–30                                                                               | 3000–4500                                                                           | ( $1.44 \times 10^7$ )<br>3000–4500                                                   | $5.28 \times 10^7$                                                                    |
| Argon Gas (L)                | 4 L                                                                                 | 9 L                                                                                 | 9 L                                                                                   | 880 L                                                                                 |

humidity from the reactants and providing a multi-spot or rastered laser ignition for uniform front propagation. Future work aims to address these challenges for advancing the technology.

## 5. Conclusions

Conclusively we demonstrate the potential of laser ignition chemical synthesis (LiChemS) in manufacturing high purity and density  $\text{Al}_2\text{O}_3$ - $\text{TiB}_2$  composites in-situ, from the starting materials of Al,  $\text{TiO}_2$  and  $\text{B}_2\text{O}_3$ , reaching an adiabatic temperature of 2643 K. LiChemS relies on a laser processing and exotherm-driven mechanism which leverages the formation of a keyhole (363  $\mu\text{m}$  crater), the ionisation of confined metal vapour in the keyhole and Marangoni convection. The absorption coefficient of the reactants was measured as 33 % and plasma was generated at the focal point for laser intensities greater than 1.13 W/ $\text{mm}^2$ , operating 10<sup>4</sup> W/ $\text{cm}^2$  below high-power welding thresholds. The manufactured composites contained traces of  $\text{Ti}_2\text{O}_3$  and no aluminoborate phases, attributed to the rapid heating during LiChemS. New reaction mechanisms were suggested for describing side reactions taking place during ignition. The skeletal and bulk densities of the PPH-FPH-LPH composites were 4010  $\text{kg/m}^3$  (96 %) and 3830  $\text{kg/m}^3$  (92 %) respectively, comparable to the ones by in-situ hot-pressing. CT scan analysis evaluated the generation of cracks within the matrix due to degassing. The surface roughness of the  $\text{Al}_2\text{O}_3$ - $\text{TiB}_2$  composites progressively reduced from 54 to 14  $\mu\text{m}$  proportionally to the effectiveness of the processing methods in drying and sintering the reactants prior to LiChemS. Porosity arranged in the form of concentric circles around the keyhole was attributed to Marangoni convection. The depth of the keyhole formed during LiChemS was measured as 360  $\mu\text{m}$ . Microstructural analysis displayed fine and clustered distribution of  $\text{TiB}_2$  and  $\text{Ti}_2\text{O}_3$  nanoparticles (10–600 nm) in the alumina matrix. The Vickers micro-Hardness of the composites was independent of load and equal to 1850 HV - 18.14  $\pm$  0.49 GPa (95 %), while the fracture toughness was 5.8 MPa  $\text{m}^{1/2}$ . The compressive strength of PPH-FPH-LPH composite was greater than alumina by 15 %. The analytical model combining Hertzian contact mechanics and impact mechanics approximated the height for performing ball drop tests. The composites could withstand 174 N before fracturing. A more detailed examination of the ballistic resistance performance of the composites will be carried out in the future work. Overall, this work demonstrates the potential of LiChemS to manufacture energy demanding materials of customised shapes and sizes, in a rapid, cost and energy efficient manner, without compromising on their physical and mechanical properties.

## Data statement

Data will be available upon request.

## Funding

This research was funded by the Defence Science and Technology Laboratory (DSTL). This research was also funded by the Engineering and Physical Sciences Research Council (EPSRC), Project Reference No. 1787225, The Medical Research Council: MRC-CIC-L42017/PO4050781788 and the Biomedical Research Centre (NIHR-20331).

## Declaration of competing interest

The authors declare that they have no known competing financial interests or personal relationships that could have appeared to influence the work reported in this paper.

## Acknowledgements

The authors would like to acknowledge the Defence Science and Technology Laboratory (DSTL) for their financial and scientific support

throughout this research. The authors also acknowledge the University of Leeds for providing the facilities for conducting the research. Special thanks to Robert Simpson SCaPE (University of Leeds), Tony Wiese MechEng (University of Leeds), Camille Hammersley MechEng (University of Leeds), Sarathkumar Loganathan (University of Leeds) and Geeta Sharma (University of Leeds).

## Appendix A. Supplementary data

Supplementary data to this article can be found online at <https://doi.org/10.1016/j.jmrt.2025.09.045>.

## References

- [1] Levashov EA, Mukasyan AS, Rogachev AS, Shtansky DV. Self-propagating high-temperature synthesis of advanced materials and coatings. *Int Mater Rev* 2017;62(4):203–39.
- [2] Azom. Alumina - aluminium oxide -  $\text{Al}_2\text{O}_3$  - a refractory ceramic oxide. 2001.
- [3] Goodfellow. Titanium diboride ( $\text{TiB}_2$ ) - properties and applications. 2001.
- [4] Goldschmid HJ. Interstitial alloys. Springer; 2013.
- [5] Mohammad Sharifi E, Karimzadeh F, Enayati MH. Synthesis of titanium diboride reinforced alumina matrix nanocomposite by mechanochemical reaction of  $\text{Al-TiO}_2\text{-B}_2\text{O}_3$ . *J Alloys Compd* 2010;502(2):508–12.
- [6] Sharifi EM, Karimzadeh F, Enayati MH. Preparation of  $\text{Al}_2\text{O}_3$ - $\text{TiB}_2$  nanocomposite powder by mechanochemical reaction between Al,  $\text{B}_2\text{O}_3$  and Ti. *Adv Powder Technol* 2011;22(4):526–31.
- [7] Khaghani-Dehaghani MA, Ebrahimi-Kahrizangi R, Setoudeh N, Nasiri-Tabrizi B. Mechanochemical synthesis of  $\text{Al}_2\text{O}_3$ - $\text{TiB}_2$  nanocomposite powder from  $\text{Al-TiO}_2\text{-H}_3\text{BO}_3$  mixture. *Int J Refract Metals Hard Mater* 2011;29(2):244–9.
- [8] Rabieizadeh A, Hadian A, Ataie AJJORM, Materials H. Preparation of alumina/titanium diboride nano-composite powder by milling assisted sol-gel method, vol. 31; 2012. p. 121–4.
- [9] Yang W, Dong SJ, Yangli AZ, Xie ZX. Synthesis of  $\text{Al}_2\text{O}_3$ - $\text{TiB}_2$  composite powder by planetary milling from  $\text{Al-TiO}_2\text{-B}_2\text{O}_3$ -Ni mixture. In: *Applied mechanics and materials*. Trans Tech Publ; 2013. p. 734–7.
- [10] Daskalakis E, Scott A, Jha A. Enhancing the ignitability of the  $\text{Al-TiO}_2\text{-B}_2\text{O}_3$  powder mixture through intensive vibratory ball milling (C:P12). *Ceram Int* 2023;49(14, Part B):24142–55.
- [11] Mousavian RT, Sharafi S, Shariat MJJoMS, Engineering. Preparation of nano-structural  $\text{Al}_2\text{O}_3$ - $\text{TiB}_2$  in-situ composite using mechanically activated combustion synthesis followed by intensive milling 2011;8(2):1–9.
- [12] Li J, Cai Z, Guo H, Xu B, Li L. Characteristics of porous  $\text{Al}_2\text{O}_3$ - $\text{TiB}_2$  ceramics fabricated by the combustion synthesis. *J Alloys Compd* 2009;479(1):803–6.
- [13] Wang D. Effects of additives on combustion synthesis of  $\text{Al}_2\text{O}_3$ - $\text{TiB}_2$  ceramic composite. *J Eur Ceram Soc* 2009;29(8):1485–92.
- [14] Plovnick RH, Richards EAJMr. New combustion synthesis route to  $\text{TiB}_2$ - $\text{Al}_2\text{O}_3$  2001;36(7–8):1487–93.
- [15] Kimura I, Hotta N, Hiraoka Y, Saito N, Yokota Y. Sintering and characterization of  $\text{Al}_2\text{O}_3$ - $\text{TiB}_2$  composites. *J Eur Ceram Soc* 1989;5(1):23–7.
- [16] Kecskes LJ, Niiier A, Kottke T, Logan KV, Villalobos GRJotACS. Dynamic consolidation of combustion-synthesized alumina-titanium diboride composite. *Ceramics* 1996;79(10):2687–95.
- [17] Meyers MA, Olevsky EA, Ma J, Jamet M. Combustion synthesis/densification of an  $\text{Al}_2\text{O}_3$ - $\text{TiB}_2$  composite. *Materials Science and Engineering: A* 2001;311(1):83–99.
- [18] Liu G, Yan D, Zhang JJJoWUoT-MSE. Microstructure and mechanical properties of  $\text{TiB}_2$ - $\text{Al}_2\text{O}_3$  composites 2011;26(4):696–9.
- [19] Rabieizadeh A, Ataie A, Hadian AM. Sintering of  $\text{Al}_2\text{O}_3$ - $\text{TiB}_2$  nano-composite derived from milling assisted sol-gel method. *Int J Refract Metals Hard Mater* 2012;33:58–64.
- [20] Yu Popov A, Sivak AA, Yu Borodianska H, Shabalin IL. High toughness  $\text{TiB}_2$ - $\text{Al}_2\text{O}_3$  composite ceramics produced by reactive hot pressing with fusible components. *Adv Appl Ceram* 2015;114(3):178–82.
- [21] Dorri Moghadam A, Omrani E, Lopez H, Zhou L, Sohn Y, Rohatgi PK. Strengthening in hybrid alumina-titanium diboride aluminum matrix composites synthesized by ultrasonic assisted reactive mechanical mixing. *Materials Science and Engineering: A* 2017;702:312–21.
- [22] Kurtoglu A. Aluminum oxide and titanium diboride reinforced metal matrix composite and its mechanical properties. Thesis, citeseer. 2004.
- [23] Tang W, Fu Z, Zhang J, Wang W, Wang H, Wang Y, Zhang QJPT. Fabrication and characteristics of  $\text{TiB}_2$ / $\text{Al}_2\text{O}_3$  core/shell particles by hybridization 2006;167(3):117–23.
- [24] Xu J, Zou B, Tao S, Zhang M, Cao X. Fabrication and properties of  $\text{Al}_2\text{O}_3$ - $\text{TiB}_2$ -TiC/Al metal matrix composite coatings by atmospheric plasma spraying of SHS powders. *J Alloys Compd* 2016;672:251–9.
- [25] Cheng H, Li Z, Shi YJSE. Microstructure and wear resistance of  $\text{Al}_2\text{O}_3$ - $\text{TiB}_2$  composite coating deposited by axial plasma spraying 2008;24(6):452–7.
- [26] Chatterjee S, Shariff SM, Datta Majumdar J, Roy Choudhury A. Development of nano-structured  $\text{Al}_2\text{O}_3$ - $\text{TiB}_2$ -TiN coatings by combined SHS and laser surface alloying. *Int J Adv Des Manuf Technol* 2008;38(9):938–43.
- [27] Eskandari H, Taheri RJPMS. A novel technique for development of aluminum alloy matrix/ $\text{TiB}_2$ / $\text{Al}_2\text{O}_3$  hybrid surface nanocomposite by friction stir processing 2015;11:503–8.



- [28] Sajedi Alvar F, Heydari M, Kazemzadeh A, Vaezi M, Nikzad L. Al<sub>2</sub>O<sub>3</sub>-TiB<sub>2</sub> nanocomposite coating deposition on titanium by air plasma spraying. *Mater Today Proc* 2018;5(7):15739–43. Part 3.
- [29] Borovinskaya JJP, Chemistry A. Chemical classes of the SHS processes and materials 1992;64(7):919–40.
- [30] Mossino P. Some aspects in self-propagating high-temperature synthesis. *Ceram Int* 2004;30(3):311–32.
- [31] Rosa R, Veronesi P, Casagrande A, Leonelli CJJoA, Compounds. Microwave ignition of the combustion synthesis of aluminides and field-related effects, vol. 657; 2016. p. 59–67.
- [32] Clark D, Ahmad I, Dalton RJMS, A E. Microwave ignition and combustion synthesis of composites 1991;144(1–2):91–7.
- [33] Logan K, Sparrow J, McLemore W. Experimental modeling of particle-particle interactions during SHS of TiB 2-Al 2 O 3. In: *Combustion and plasma synthesis of high-temperature materials*; 1990.
- [34] Sundaram V, Logan K, Speyer R. Aluminothermic reaction path in the synthesis of a TiB 2–Al 2 O 3 composite. *J Mater Res* 1997;12(7):1681–4.
- [35] Adin MŞ, Adin H. Machining eco-friendly jute fiber-reinforced epoxy composites using specially produced cryo-treated and untreated cutting tools 2024;16(23): 3329.
- [36] Munro RG. Material properties of titanium diboride. *Journal of Research of the National Institute of Standards and Technology* 2000;105(5):709.
- [37] Suleiman B, Zhang H, Ding Y, Li Y. Microstructure and mechanical properties of cold sintered porous alumina ceramics. *Ceram Int* 2022;48(10):13531–40.
- [38] Shuai X, Zeng Y, Li P, Chen J. Fabrication of fine and complex lattice structure Al<sub>2</sub>O<sub>3</sub> ceramic by digital light processing 3D printing technology. *J Mater Sci* 2020;55(16):6771–82.
- [39] He J, Wang M. Ballistic performance of laminated functionally graded composites of TiB<sub>2</sub>-based ceramic and Ti-6Al-4V alloy against 14.5 mm heavy machine gun AP of impact velocity 990 m/s. In: *2015 44th international conference on sustainable energy and environmental engineering*. Atlantis Press; 2016.
- [40] Shanazari H, Liaghat G, Feli S, Hadavinia H. Analytical and experimental study of high-velocity impact on ceramic/nanocomposite targets. *J Compos Mater* 2017;51(27):3743–56.
- [41] Chen Y, Chu C, Chuang W, Lee S, Lee K. A study of ceramic composite materials for bullet-proof optimization by using Taguchi method. In: *16th international conference on composite materials*; 2007.
- [42] Rozenberg Z, Yeshurun Y. The relation between ballistic efficiency and compressive strength of ceramic tiles. *Int J Impact Eng* 1988;7(3):357–62.
- [43] Zhai J, Zhou M. Micromechanical modeling of mixed-mode crack growth in ceramic composites. In: *Mixed-mode crack behavior*. ASTM International; 1999.
- [44] Gilde GA, Adams JW. Processing and ballistic performance of Al<sub>2</sub>O<sub>3</sub>/TiB<sub>2</sub> composites. ARMY RESEARCH LAB ABERDEEN PROVING GROUND MD; 2005.
- [45] Abfalter G, Brar N, Jurick D. Determination of the dynamic unload/reload characteristics of ceramics. DAYTON UNIV OH RESEARCH INST; 1992.
- [46] Silva MV, Stainer D, Al-Qureshi HA, Montedo ORK, Hotza D. Alumina-based ceramics for armor application: mechanical characterization and ballistic testing. *Journal of Ceramics* 2014;2014(1):618154.
- [47] Marshall DB, Lawn BRJMTiMS, Engineering AS. Indentation of brittle materials, vol. 889; 1986. p. 26–46.
- [48] Ghaednia H, Wang X, Saha S, Xu Y, Sharma A, Jackson RL. A review of elastic-plastic contact mechanics. *Appl Mech Rev* 2017;69(6).
- [49] Hertzberg RW, Vinci RP, Hertzberg JL. Deformation and fracture mechanics of engineering materials. John Wiley & Sons; 2020.
- [50] Adin H, Adin MŞ. Effect of particles on tensile and bending properties of jute epoxy composites 2022;64(3):401–11.
- [51] Rachid HB, Noureddine D, Benali B, Adin MŞ. Effect of nanocomposites rate on the crack propagation in the adhesive of single lap joint subjected to tension. *Mech Adv Mater Struct* 2024;31(25):6898–906.
- [52] Adin, H., Akgül, S. and Adin, M.Ş. Effect of silver nanopowder addition on mechanical properties of silver-copper alloy used in the jewellery industry. 0(0), p.09544089251316320.
- [53] Tavakolian P, Mandelis A. Perspective: principles and specifications of photothermal imaging methodologies and their applications to non-invasive biomedical and non-destructive materials imaging. *J Appl Phys* 2018;124(16): 160903.
- [54] Ahmed FE, Hashaikeh R, Hilal N. Solar powered desalination – technology, energy and future outlook. *Desalination* 2019;453:54–76.
- [55] Biffi CA, Bassani P, Sajedi Z, Giuliani P, Tuissi A. Laser ignition in self-propagating high temperature synthesis of porous NiTiInol shape memory alloy. *Mater Lett* 2017;193:54–7.
- [56] Li YX, Hu JD, Liu YH, Yang Y, Guo ZX. Effect of C/Ti ratio on the laser ignited self-propagating high-temperature synthesis reaction of Al–Ti–C system for fabricating TiC/Al composites. *Mater Lett* 2007;61(22):4366–9.
- [57] Li YX, Hu JD, Wang HY, Guo ZX. Study of TiC/Ni<sub>3</sub>Al composites by laser ignited self-propagating high-temperature synthesis (LISHS). *Chem Eng J* 2008;140(1): 621–5.
- [58] Li Z, Feng G, Wang S, Feng S. High-efficiency joining of Cf/Al composites and TiAl alloys under the heat effect of laser-ignited self-propagating high-temperature synthesis. *J Mater Sci Technol* 2016;32(11):1111–6.
- [59] Hunt EM, Plantier KB, Pantoya ML. Nano-scale reactants in the self-propagating high-temperature synthesis of nickel aluminide. *Acta Mater* 2004;52(11):3183–91.
- [60] An Y-J, Zhu L, Jin S-H, Lu J-J, Liu X-Y. Laser-ignited self-propagating sintering of AlCrFeNiSi high-entropy alloys: an improved technique for preparing high-entropy. *Alloys* 2019;9(4):438.
- [61] Liu J, Wen P. Metal vaporization and its influence during laser powder bed fusion process. *Mater Des* 2022;215:110505.
- [62] Cunningham R, Zhao C, Parab N, Kantzos C, Pauza J, Fezzaa K, Sun T, Rollett AD. Keyhole threshold and morphology in laser melting revealed by ultrahigh-speed x-ray imaging 2019;363(6429):849–52.
- [63] Rai R, Elmer JW, Palmer TA, DebRoy T. Heat transfer and fluid flow during keyhole mode laser welding of tantalum, Ti–6Al–4V, 304L stainless steel and vanadium. *J Phys Appl Phys* 2007;40(18):5753.
- [64] Fabbro R. Melt pool and keyhole behaviour analysis for deep penetration laser welding. *J Phys Appl Phys* 2010;43(44):445501.
- [65] Volpp J, Zaiss F, Hagenlocher C, Graf T. Surface tension derivation from laser-generated keyholes. *J Laser Appl* 2024;36(3).
- [66] Loganathan S, Santhanakrishnan S, Bathe R, Arunachalam M. Prediction of femtosecond laser ablation profile on human teeth. *Laser Med Sci* 2019;34(4): 693–701.
- [67] Kumi-Barimah E, Penhale-Jones R, Salimian A, Upadhyaya H, Hasnath A, Jose G. Phase evolution, morphological, optical and electrical properties of femtosecond pulsed laser deposited TiO<sub>2</sub> thin films. *Sci Rep* 2020;10(1):10144.
- [68] Rupp B, Holt JB, Wong JJC. The calculation and analysis of the adiabatic temperature of solid combustion reactions 1992;16(4):377–86.
- [69] Meyers M, Olevsky E, Ma J, Jamet M. Combustion synthesis/densification of an Al<sub>2</sub>O<sub>3</sub>-TiB<sub>2</sub> composite. *Materials Science and Engineering: A* 2001;311(1–2): 83–99.
- [70] Bailey BJ, Kellner K. The thermal conductivity of liquid and gaseous argon. *Physica* 1968;39(3):444–62.
- [71] Aloub L, Lishchuk SV. Bulk viscosity of gaseous argon from molecular dynamics simulations. *Phys Rev* 2022;105(5):054135.
- [72] Johns DJ. Thermal stress analyses. Elsevier; 2013.
- [73] Wellen RMR, Canedo EL. On the Kissinger equation and the estimate of activation energies for non-isothermal cold crystallization of PET. *Polym Test* 2014;40:33–8.
- [74] Li Y, Huang S, Bai P, Liu B, Wang J. Effect of Ti/Si ratio on the products of laser igniting self-propagating high-temperature synthesis in Cu–Ti–Si system. *J Alloys Compd* 2013;548:245–8.
- [75] Li Y, Bai P, Liu B, Wang J. Effect of Al<sub>2</sub>O<sub>3</sub> content on the synthesized products by the laser ignited self-propagating high-temperature synthesis reaction of Al<sub>2</sub>O<sub>3</sub>-Ti–C system. *Int J Refract Metals Hard Mater* 2012;34:53–6.
- [76] Feng G-j, Li Z-r, Feng S-c, Shen Z-k. Effect of Ti–Al content on microstructure and mechanical properties of Cf/Al and TiAl joint by laser ignited self-propagating high-temperature synthesis. *Trans Nonferrous Metals Soc China* 2015;25(5): 1468–77.
- [77] Qin L, Hu J, Cui C, Wang H, Guo Z. Effect of Al content on reaction laser sintering of Ni–Al powder. *J Alloys Compd* 2009;473(1):227–30.
- [78] Mousavian RT, Sharafi S, Shariat MH. Microwave-assisted combustion synthesis in a mechanically activated Al–TiO<sub>2</sub>-H<sub>3</sub>BO<sub>3</sub> system. *Int J Refract Metals Hard Mater* 2011;29(2):281–8.
- [79] Haghighi RR, Chatterjee S, Vyas A, Kumar P, Thulkar SJMP X. -ray attenuation coefficient of mixtures: inputs for dual-energy CT 2011;38(10):5270–9.
- [80] Schulz LJAIP. The experimental study of the optical properties of metals and the relation of the results to the Drude free electron theory 1957;6(21):102–44.
- [81] Loganathan S, Santhanakrishnan S, Bathe R, Arunachalam M. Surface processing: an Elegant Way to enhance the femtosecond laser ablation rate and ablation efficiency on human teeth. *Laser Surg Med* 2019;51(9):797–807.
- [82] Ray SPJotacs. Preparation and characterization of aluminum borate 1992;75(9): 2605–9.
- [83] Li Y, Wang L, Li J, Chen C, Li X, Tuo B. Nucleation mechanisms of titanium oxide particles at high temperature based on cluster-assisted nucleation. *J Mater Res Technol* 2022;19:578–90.
- [84] Affi M, Abdel-Aziz M, Yahia I, Fadel M, Wahab LJJoA, compounds. Transport properties of polycrystalline TiO<sub>2</sub> and Ti<sub>2</sub>O<sub>3</sub> as semiconducting oxides 2008;455(1–2):92–7.
- [85] Valeeva AA, Nazarova SZ, Rempel AAJoA, Compounds. Nanosize effect on phase transformations of titanium oxide Ti<sub>2</sub>O<sub>3</sub>, vol 817; 2020. 153215.
- [86] Daskalakis E, Jha A, Scott A, Hassanpour A. Phase and microstructural analysis of in-situ derived alumina-TiB<sub>2</sub> composites. In: *TMS 2022 151st Annual Meeting & exhibition Supplemental Proceedings*. Springer; 2022. p. 49–59.
- [87] Chen T, Gong B, Tang Ca. Origin and evolution of cracks in the Glaze surface of a ceramic during the cooling process 2023;16(16):5508.
- [88] Daskalakis E, Scott A, Jha A. Enhancing the ignitability of the Al–TiO<sub>2</sub>-B<sub>2</sub>O<sub>3</sub> powder mixture through intensive vibratory ball milling (C:P12). *Ceram Int* 2022.
- [89] Leriche A, Hampshire S, Cambier FJRiMS, Engineering M. Sintering of ceramics. 2017.
- [90] Liu B, Jiang G, Mei X, Wang K, Wang J. Formation of porous structure with subspot size under the irradiation of picosecond laser pulses. *J Nanomater* 2013;2013.
- [91] Nuismer RJJof. An energy release rate criterion for mixed mode. fracture 1975;11(2):245–50.